J. Fluid Mech. (2008), *vol.* 615, *pp.* 445–475.
doi:10.1017/S0022112008004047 Printed in the United Kingdom

Pressure-gradient-dependent logarithmic laws in sink flow turbulent boundary layers

SHIVSAI AJIT DIXIT AND O. N. RAMESH

Department of Aerospace Engineering, Indian Institute of Science, Bangalore 560012, India

(Received 22 April 2008 and in revised form 18 August 2008)

Experiments were done on sink flow turbulent boundary layers over a wide range of streamwise pressure gradients in order to investigate the effects on the mean velocity profiles. Measurements revealed the existence of non-universal logarithmic laws, in both inner and defect coordinates, even when the mean velocity descriptions departed strongly from the universal logarithmic law (with universal values of the Kármán constant and the inner law intercept). Systematic dependences of slope and intercepts for inner and outer logarithmic laws on the strength of the pressure gradient were observed. A theory based on the method of matched asymptotic expansions was developed in order to explain the experimentally observed variations of log-law constants with the non-dimensional pressure gradient parameter ($\Delta_p = (\nu/\rho U_\tau^3)\mathrm{d}p/\mathrm{d}x$). Towards this end, the system of partial differential equations governing the mean flow was reduced to inner and outer ordinary differential equations in self-preserving form, valid for sink flow conditions. Asymptotic matching of the inner and outer mean velocity expansions, extended to higher orders, clearly revealed the dependence of slope and intercepts on pressure gradient in the logarithmic laws.

1. Introduction

The effects of strong streamwise favourable pressure gradients (FPG) on the mean velocity profile of a turbulent boundary layer (TBL) have been reported by many researchers in the literature. It is known that the mean velocity profiles in such flows exhibit departures from the universal logarithmic law (see e.g. Patel 1965; Kline *et al.* 1967; Patel & Head 1968; Jones & Launder 1972; Spalart 1986; Fernholz & Warnack 1998). For such strong pressure gradients, the total shear stress in the near-wall region can no longer be treated constant as in the case of a zero-pressure-gradient (ZPG) turbulent boundary layer. Instead a linear variation of the total shear stress (see Townsend 1976) must be considered as a better approximation to the situation.

Patel & Head (1968) have given a closed form expression for the mean velocity profile in wall variables for such strong pressure gradient flows. This expression has been obtained by using a mixing length approach in conjunction with a linear total stress variation and involves the non-dimensional shear stress gradient as a parameter. The expression predicts the mean velocity profiles in adverse pressure gradients (APG) reasonably well. However for FPG flows, Narasimha & Sreenivasan (1973) have pointed out that it is not possible to evaluate this expression beyond certain low values of y_+ (of the order of 100). Moreover, the total stress gradient in the analysis of Patel & Head (1968) is an adjustable parameter so as to give a good fit to the experimental data.

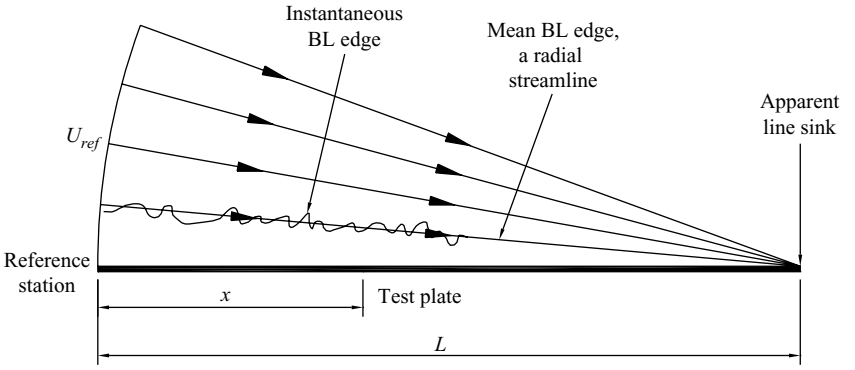

FIGURE 1. Two-dimensional sink flow turbulent boundary layer.

Other researchers such as Spalart & Leonard (1986) and Nickels (2004) have also noted departures of the mean velocity profile from the universal logarithmic law in pressure gradient flows and have proposed variations of apparent slope and intercept of the logarithmic law with pressure gradient.

A critical survey of the FPG flows of Kline *et al.* (1967), Patel & Head (1968) and Fernholz & Warnack (1998) shows strong departures of the mean velocity profiles from the universal logarithmic law. Even so, it is interesting to note that the mean velocity variation in such cases appears to be logarithmic (with the same slope in the so-called inner and defect scalings) – albeit different from the universal form. However it is important to note that in all these flows, the conditions change rather rapidly in the streamwise direction. This implies that each of these boundary layers is essentially in a non-equilibrium state, in the sense of Clauser (1956). Thus the mean velocity profiles and the other integral quantities are expected to depend on a combined effect of the local pressure gradient and the pressure gradient history. The presence of history effects is likely to render any local scaling argument of little use in such non-equilibrium boundary layer flows.

In order to study the effect of local pressure gradient on the mean velocity profile in a compartmentalized fashion, it is therefore necessary as a first step to focus attention on those flows where the history effects are absent or are negligibly small. Such flows are termed equilibrium flows by Clauser (1954). Motivation for the idea of equilibrium comes from an analogy to the self-similar Falkner–Skan profiles in laminar boundary layers. Extended to turbulent boundary layers, the idea of self-preservation (in the sense of Townsend 1976) connotes the self-similarity of mean velocity and shear stress profiles under proper normalization. We shall use the words equilibrium, self-preservation and self-similarity interchangeably in what follows.

Townsend (1956, 1976) and Rotta (1962) have shown that the turbulent boundary layer flow in a convergent channel bounded by two smooth plane surfaces, the so-called sink flow, satisfies the conditions for exact or strict self-preservation. Thus the sink flow TBL would be an ideal candidate for studying the effects of local FPG. In addition, the sink flow TBL has many other interesting properties (see Townsend 1976), some of which are described here. First, the mean entrainment is zero for a sink flow TBL. Consequently the mean edge of the boundary layer becomes a streamline, with all the streamlines being radial lines of the convergent geometry (see figure 1). This results in the boundary layer thickness and the other integral thicknesses decreasing linearly in the streamwise direction. Secondly, the Reynolds number, no

matter how it is defined, remains constant in the streamwise direction. Also the acceleration parameter K, the pressure gradient parameter Δ_p, respectively defined as

$$K = \frac{\nu}{U_\infty^2}\frac{\mathrm{d}U_\infty}{\mathrm{d}x}, \tag{1.1}$$

$$\Delta_p = \frac{\nu}{\rho U_\tau^3}\frac{\mathrm{d}p}{\mathrm{d}x} = \frac{-K}{(C_f/2)^{3/2}}, \tag{1.2}$$

and the skin friction coefficient C_f all remain constant in the streamwise direction. Here U_∞ is the free-stream velocity and $U_\tau = \sqrt{\tau_w/\rho}$ is the friction velocity. All these properties are useful indicators for checking the attainment of a sink flow configuration in experiments.

Launder & Jones (1969) have given a calculation procedure for sink flow TBLs based on a mixing length model. Following this, Jones & Launder (1972) have done experimental studies on sink flow. However, their primary interest was centred on relaminarization and hence their data present a limited range of pressure gradients (in terms of the values of Δ_p) closer to the relaminarization condition. Direct numerical simulation (DNS) of sink flow by Spalart (1986) also covers a range of Δ_p values similar to that of Jones & Launder (1972). Sink flow experiments of Jones, Marusic & Perry (2001) present data for a range of Δ_p values which are fairly low (i.e. closer to the ZPG situation) since their main aim was to test the closure hypothesis of Perry, Marusic & Li (1994). See also Perry, Marusic & Jones (2002) in this connection where a closure model for flows approaching equilibrium is discussed with special reference to the sink flow. There exist no other systematic experimental data on sink flows covering a broad range of pressure gradients (from the ZPG limit to the relaminarization limit).

The present work was hence planned to systematically explore the mean velocity scaling in sink flow TBLs over a wider range of pressure gradients. Details of the experimental setup and procedures are given in § 2 while results from the present experiments are presented in § 3. A corresponding theory based on the method of matched asymptotic expansions is given in § 4. Comparison of the theory with the results of the present experiments and those of some experimental and numerical studies from the literature is made in § 5 and the conclusions are presented in § 6.

It must be mentioned here that the asymptotic analysis presented in § 4 is of classical type (i.e. on the lines of Millikan 1938) involving a two-layer description and should be contrasted with the work of George & Castillo (1997) (where the so-called Asymptotic Invariance Principle is developed). Furthermore, terms such as equilibrium, self-preservation and self-similarity used in the present work are also to be understood in the classical sense (Townsend 1976; Clauser 1956).

2. Experimental setup

2.1. *Experimental facility and pressure, velocity measurements*

Experiments were done in a low-speed wind tunnel at the Department of Aerospace Engineering, Indian Institute of Science. The tunnel is a suction-type open-return wind tunnel with test-section size of 300 mm × 300 mm over a working length of about 3 m. Sidewalls are slightly divergent to accommodate boundary layer growth on them. Suitable honeycomb and screens ahead of an 11:1 contraction ensure nearly uniform flow at the entry to the test-section with a free-stream turbulence level of less than 0.3%. The test-section is followed by a diffuser downstream. A fan is located downstream of the diffuser and is driven by a 10 HP, 3-phase induction motor.

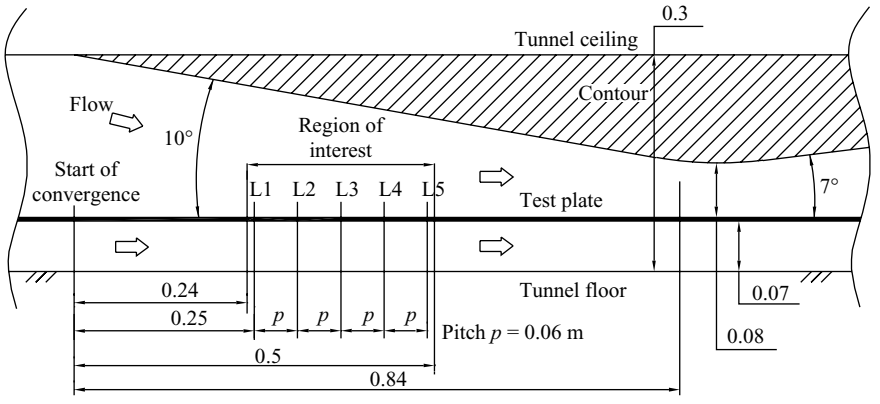

FIGURE 2. Schematic of the experimental sink flow setup. All dimensions in metres.

Velocity in the test-section can be varied by changing the fan speed using a variable frequency drive. The maximum velocity is about 33 m s^{-1}.

All the present boundary layer measurements were done on a smooth, highly polished test-plate made from duralumin (300 mm × 2000 mm × 5 mm). The plate was mounted rigidly at a height of 70 mm from the floor of the test-section. For pressure measurements, static pressure holes of 0.7 mm diameter were provided at 20 mm intervals along the centreline of the plate. A number of flush-mounted removable teflon plugs (19 mm diameter) were provided in the plate for skin friction measurement using the surface hot-wire (SHW) technique. These plugs were located on a line parallel to the centreline of the plate with an offset of 50 mm. The plate was polished with all the plugs in place so that the plugs were flush with the surface. The boundary layer was tripped by a rough emery cloth strip (15 mm width, 2 mm height and 300 mm span) which was stuck 10 mm downstream of the leading edge to hasten transition to turbulence.

The roof of the test-section was contoured in order to generate the two-dimensional sink flow configuration as shown in figure 2. The contour consisted of a 10° convergence followed by a 7° divergence. Absence of separation on both the roof and the test-plate in the divergent region was checked by tuft flow visualization. The central longitudinal slot in the contoured roof provided access for measurements along the centreline of the plate. All gaps, however small, were carefully sealed.

The static pressure coefficient C_p is defined as

$$C_p = \frac{p - p_{ref}}{\frac{1}{2}\rho U_{ref}^2}, \tag{2.1}$$

where the reference station is at the start of the convergence (see figures 1 and 2). It can be shown, using an inviscid flow assumption that

$$C_p = 1 - \frac{L^2}{(L - x)^2}, \tag{2.2}$$

where x and L are as shown in figure 1. For the measured C_p distribution, L may be obtained from (2.2), and in the present case is about 1.44 m (see figure 3*a*). This differs slightly from the actual value of L, which is 1.35 m, as obtained from the geometry of the contour. This difference is attributed to the virtual origin effect presumably arising

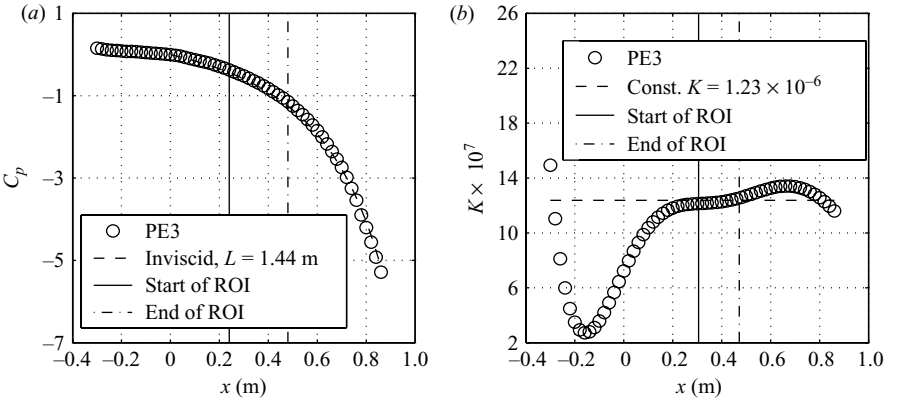

FIGURE 3. (*a*) Streamwise distribution of C_p for the present experiment PE3, and (*b*) streamwise distribution of the acceleration parameter K for experiment PE3 and identification of the region of interest (ROI). Symbol sizes represent typical uncertainty.

due to the longitudinal curvature of streamlines at the beginning of the convergent section.

Figure 3(*a*) shows the distribution of pressure coefficient C_p along the length of the test-plate for a representative present experiment PE3 (for details see table 1 below). As can be expected from (2.2), the C_p distribution was found to be invariant with changes in reference speed. Figure 3(*b*) shows the streamwise distribution of the acceleration parameter K, as defined by (1.1), for the same experiment. In figure 3(*b*) it can be seen that in the region between $x = 240$ mm and $x = 480$ mm, K is constant to within $\pm 3\%$ of the average value over that region. This is the region of interest (ROI) for the present study. In the ROI, five streamwise stations (denoted as L1 to L5 in figure 2) were chosen for measurements. In all, five different pressure gradients (designated PE1 to PE5) were investigated at these stations.

The mean velocity profiles were measured by a round Pitot tube (outer diameter of 0.6 mm) using a projection manometer with a least count of 0.1mm of methanol. The Pitot displacement correction suggested by MacMillan (1956) was always applied. For traversing the Pitot tube normal to the plate, a dial-type height gauge (Mitutoyo) with a least count of 0.01 mm, was used.

2.2. *Measurement of skin friction by the SHW technique*

In order to measure the skin friction in relatively strong FPGs, it was considered necessary to employ a method which did not depend on the universal logarithmic law. This consideration excludes use of the Clauser chart method (Clauser 1954) and the Preston tube (Patel 1965). More recently Warnack & Fernholz (1998) have successfully used SHW technique for measurement of skin friction in their experiments. These experiments involved turbulent boundary layers subjected to strong FPGs, involving relaminarization in some cases. Hence, it was decided to use this method for the measurement of skin friction in the present experiments. Descriptions of the SHW technique can be found in Bradshaw & Gregory (1959), Fernholz *et al.* (1996) and Fernholz (2006). The two-dimensional momentum integral equation (MIE) was used for cross-checking the skin friction and for verifying the two-dimensionality of the mean flow for one representative present experiment.

For implementing the SHW technique, each of the teflon plugs in the ROI was fitted with two sharp needles 4 mm apart, with their tips projecting out from the top

surface of the plug. Pt–Rh Wollaston wire (5 μm core diameter) was soldered to the tips, etched over the required length and then taken down close to the surface of the plug by carefully pulling down both the needles simultaneously. The active length l of the wire was such that $l_+ = lU_\tau/\nu$ varied from 8 to 35 over the entire range of experiments. Each sensor was calibrated *in situ* in the ZPG turbulent boundary layer flow against a Preston tube (outer diameter of 1.65 mm), twice – once before and once after the sink flow measurement. For the Preston tube, the calibration given by Patel (1965) was used. For the SHW technique, it is required that the wire always resides in the law-of-the-wall region. However, to be on the safer side, we have ensured that the wire always resides in the viscous sublayer. A way to confirm this, during its calibration in a ZPG, was to examine its calibration equation. A general calibration equation for heat-transfer-based skin friction gauges can be written as $E^2 = A + B(\tau_w)^n$ where $n = 1/3$ for hot-film gauges. For a SHW sensor located in the viscous sublayer n can be expected to be close to 0.5. Thus from the calibration of the SHW gauge, if n is found to be close to 0.5, then we can infer, with some confidence, that the gauge resides in the viscous sublayer in ZPG flow. For all SHW sensors, n was ensured to be close to 0.5. It can be expected that the viscous sublayer is smaller in extent (in terms of y_+) in a ZPG flow than in a sink flow (see e.g. Nickels 2004). Hence this exercise gave confidence that the SHW sensor was indeed placed inside the viscous sublayer in the sink flow as well. This was further corroborated by the momentum integral balance to be discussed in the next section (see figure 5*a*).

Several validation checks were carried out in the ZPG to assess the quality and repeatability of the SHW technique. During these validation checks, C_f could always be determined (with SHW in ZPG) to within $\pm 2\%$ of the corresponding Preston-tube value which itself contains a maximum uncertainty of about $\pm 1.5\%$ (see Patel 1965). Hence, the cumulative uncertainty in C_f obtained by the SHW was about $\pm 3.5\%$ which agrees well with the uncertainty for the SHW technique quoted in the literature (see e.g. Fernholz *et al.* 1996; Fernholz 2006). However, in view of the lower flow speeds in some of the present sink flow cases and the associated free convection effects, the uncertainty band can be expected to be $\pm 5\%$. Each SHW sensor was operated by a constant-temperature hot-wire anemometer (AMB-717) and a signal conditioner (AMC-717) manufactured by Sunshine Industries, Bangalore. An overheat ratio in the range of 1.2 to 1.4 was used for all the sensors. An amplification factor of 50 was used for the fluctuating component of the signal to improve its dynamical range. SHW data were acquired at a sampling rate of 5 kHz for 5 s using an IOtech DaqBook (2000 Series-16 bit, 200 kHz Data Acquisition System) and data acquisition software DASYLAB (version 7.0).

3. Results of the present experiments

3.1. *Sink flow attainment and two-dimensionality of the mean flow*

Table 1 summarizes the results of all the five present experiments corresponding to five different FPGs. The values of all the parameters are averaged over the last three stations, namely L3, L4 and L5, where the parameters were found to approach an asymptotically constant value corresponding to the sink flow.

Table 2 summarizes the results for a typical experiment PE2 at all the five streamwise locations L1 to L5 in the ROI. Here Δ stands for the Clauser thickness and G stands for the Clauser parameter, both to be formally defined in § 5.4; $\delta_+ = \delta U_\tau/\nu$ is the ratio of the outer length scale to the inner length scale. The velocity scale in all other Reynolds numbers is U_∞.

Data set	K	C_f	Δ_p	$R_{\delta_{99.5}}$	R_{δ^*}	R_θ	H	G
PE1	7.71×10^{-7}	0.00401	−0.0086	17924	1794	1337	1.342	5.689
PE2	9.45×10^{-7}	0.00403	−0.0104	15061	1516	1119	1.355	5.835
PE3	1.23×10^{-6}	0.00416	−0.0129	11652	1215	879	1.383	6.070
PE4	1.74×10^{-6}	0.00430	−0.0175	8021	889	612	1.453	6.722
PE5	2.90×10^{-6}	0.00433	−0.0288	4817	614	393	1.563	7.750

TABLE 1. Details of integral parameters in all the present experiments (averaged over the last three measurement stations L3 to L5).

Station	U_∞ (m s^{-1})	U_τ (m s^{-1})	C_f SHW	C_f MIE	$\delta_{99.5}$ (mm)	δ^* (mm)	θ (mm)	Δ (mm)
L1	13.30	0.601	0.00408	0.00437	16.46	1.78	1.31	39.41
L2	13.98	0.631	0.00408	0.00394	15.60	1.66	1.22	36.75
L3	14.76	0.666	0.00408	0.00414	15.39	1.56	1.15	34.54
L4	15.66	0.701	0.00401	0.00393	14.20	1.44	1.06	32.26
L5	16.70	0.748	0.00401	0.00404	13.66	1.35	1.00	30.20

Station	$R_{\delta_{99.5}}$	R_{δ^*}	R_θ	R_Δ	δ_+	H	G
L1	14589	1578	1162	34936	659	1.358	5.838
L2	14540	1547	1142	34252	657	1.355	5.802
L3	15150	1534	1134	33991	684	1.353	5.780
L4	14827	1508	1111	33671	664	1.356	5.868
L5	15205	1505	1110	33618	681	1.355	5.858

TABLE 2. Details of a typical present experiment PE2 at all the five measurement stations L1 to L5.

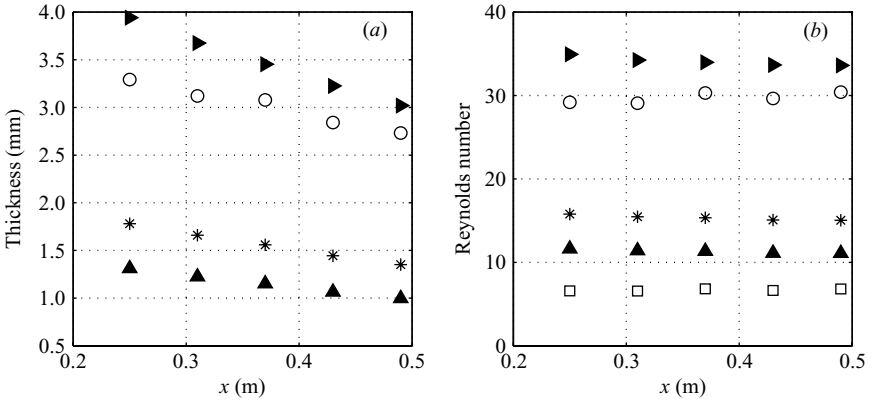

FIGURE 4. Streamwise variations of various integral flow parameters for the present experiment PE2. (*a*) Thickness: ○, $0.2 \times \delta_{99.5}$; ∗, δ^*; ▲, θ; ►, $\Delta \times 10^{-1}$. (*b*) Reynolds number: ○, $0.2 \times R_{\delta_{99.5}} \times 10^{-2}$; ∗, $R_{\delta^*} \times 10^{-2}$; ▲, $R_\theta \times 10^{-2}$; ►, $R_\Delta \times 10^{-3}$; □, $\delta_+ \times 10^{-2}$.

Figure 4(*a*, *b*) shows the streamwise variations of various integral parameters for experiment PE2. Figure 4(*a*) shows the streamwise variations of various boundary layer thicknesses. It can be seen that all the thicknesses exhibit a fairly linear decrease with the streamwise coordinate, as is expected in the case of sink flow TBL. Figure 4(*b*)

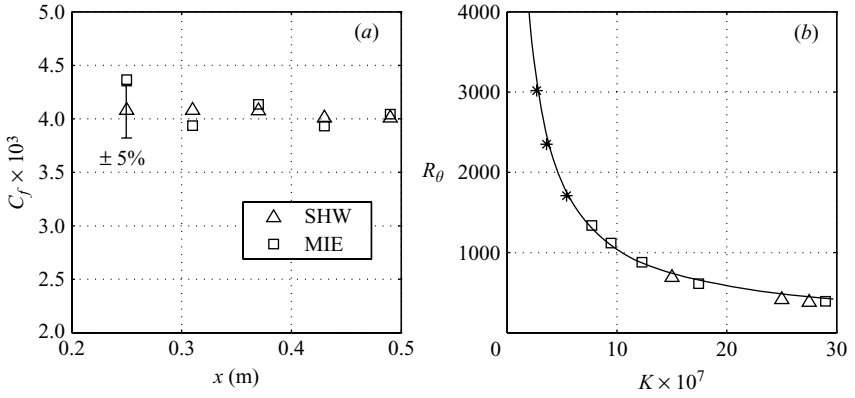

FIGURE 5. (*a*) Comparison of C_f by SHW and by MIE for the present experiment PE2. (*b*) Variation of R_θ with K. □, Present experiments; △, Spalart (1986) sink DNS; ∗, Jones *et al.* (2001) sink experiments; ——, computed precise equilibrium curve from Jones *et al.* (2001).

shows various Reynolds numbers plotted in the streamwise direction. As expected, all the Reynolds numbers remain almost constant in the streamwise direction, especially over the last three measurement stations L3, L4 and L5.

In order to assess the two-dimensionality of the mean flow, mean velocity profiles were measured at closely spaced streamwise stations to evaluate the terms in the MIE for the experiment PE2. The MIE in its full form was used without any simplifications pertaining to sink flow. Figure 5(*a*) shows a comparison of C_f obtained from the SHW with that obtained from the MIE for this experiment. The maximum difference between the SHW and the MIE, of the order of 7%, is seen at station L1. The overall good agreement between the SHW and the MIE indicates that the mean flow is reasonably two-dimensional and that the performance of the SHW sensors is quite satisfactory. Also the measured streamwise constancy of C_f seen here, as could be expected in a sink flow TBL, further confirms the integrity of the SHW measurements. Other researchers (see e.g. Bradshaw & Ferriss 1965) have noted the inaccuracies involved in using the MIE, especially in adverse pressure gradient flows, where the thick sidewall boundary layers are known to compromise the two-dimensionality of the flow. However this seems to be less of an issue in the sink flow, where due to flow acceleration, the sidewall boundary layers are expected to be thinner.

Figure 5(*b*) shows the momentum thickness Reynolds number R_θ plotted against the acceleration parameter K for all the present sink flow experiments. Data points from the present experiments lie fairly close to the computed precise equilibrium curve as scanned from figure 14 of Jones *et al.* (2001). Small differences, especially towards large values of K, may be attributed to the variation of $1/\kappa$ with pressure gradient (which will be demonstrated later in this paper) that was not taken into account by Jones *et al.* (2001) while calculating the precise equilibrium solution. In any case, figure 5(*b*) confirms the close attainment of the asymptotic sink flow configuration for all the present experiments.

Following Townsend (1976), the scaling of mean velocity in defect coordinates for a TBL can be written

$$\frac{U - U_\infty}{U_\tau} = F\left(\frac{y}{\delta}\right). \tag{3.1}$$

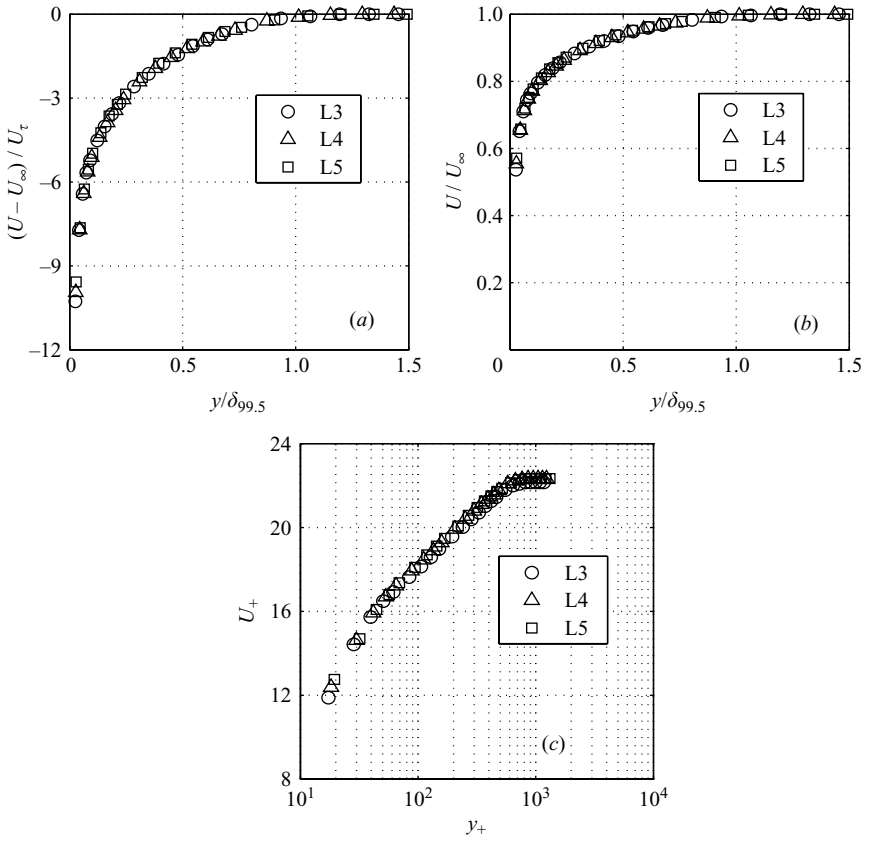

FIGURE 6. Mean velocity profiles for experiment PE2 at the last three stations L3 to L5 in the ROI. (*a*) Defect coordinates, (*b*) conventional coordinates and (*c*) inner coordinates.

For a sink flow TBL, the skin friction coefficient $C_f = 2(U_\tau/U_\infty)^2$ is constant in the streamwise direction. Hence (3.1) may now be rewritten, for sink flow, as

$$\frac{U}{U_\infty} = 1 + (C_f/2)^{1/2} F\left(\frac{y}{\delta}\right) = G\left(\frac{y}{\delta}\right). \tag{3.2}$$

Equation (3.2) is significant because it shows that for a sink flow TBL, the mean velocity profiles in conventional laminar-like coordinates (i.e. U/U_∞ and y/δ) must also be self-similar. This seemingly simple but interesting fact is perhaps not well-recognized in the literature.

Figure 6(*a–c*) shows the mean velocity profiles in defect, conventional and inner coordinates respectively, as measured at stations L3, L4 and L5 for the present experiment PE2. The trend seen in figure 6(*b*) is in agreement with the expectation from (3.2). The collapse of streamwise mean velocity profiles (also seen for other experiments, but not shown here) in all the scalings demonstrates the attainment of the sink flow configuration in the present experiments.

3.2. *Mean velocity profile results*

Figure 7 shows the mean velocity profiles from the present sink flow experiments in conventional coordinates. These profiles correspond to different values of Δ_p at the streamwise station L4 in the ROI. Also plotted is the laminar sink flow boundary

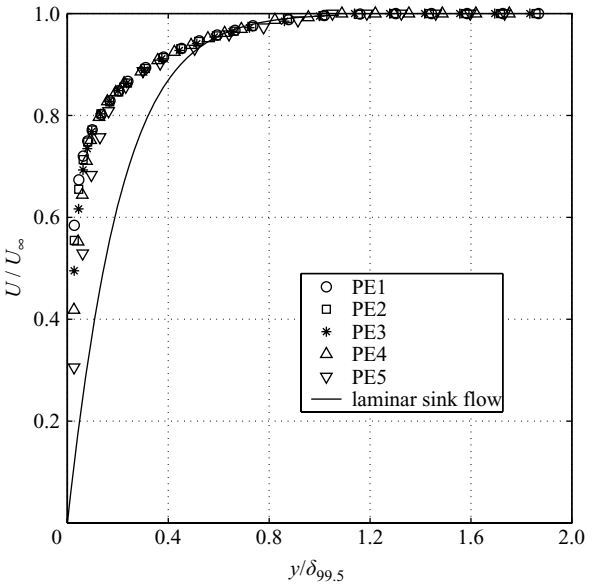

FIGURE 7. Mean velocity profiles in conventional coordinates for different pressure gradients at station L4.

layer solution which is an exact solution (see Schlichting & Gersten 2000). All the measured profiles are much fuller compared to the laminar profile as can be expected for the turbulent mean velocity profiles.

It is well-known that the mean velocity profiles of ZPG turbulent boundary layers (having different Reynolds numbers) exhibit a universal logarithmic behaviour in the overlap region when plotted in inner coordinates (i.e. U_+ and y_+). This universal logarithmic law is given by

$$U_+ = \frac{1}{\kappa_z} \ln (y_+) + C_z, \tag{3.3}$$

where $U_+ = U/U_\tau$, $y_+ = yU_\tau/\nu$, and κ_z and C_z are universal constants having values 0.41 and 5.2 respectively.

Figure 8 shows the sink flow mean velocity profiles (corresponding to those in figure 7) plotted in inner coordinates. Clearly, the profiles depart greatly from the universal logarithmic law (3.3). However a careful look reveals the following two interesting points. First, for each mean velocity profile, a logarithmic region appears to exist even when the profile has departed greatly from the universal logarithmic law. Secondly, the slope $1/\kappa$ and the inner intercept C for this new non-universal logarithmic law appear to be changing in a systematic fashion in relation to the strength of the pressure gradient. Further, each profile appears to be like a 'pure wall-flow' (see Coles 1957) when viewed with respect to its own logarithmic region as the datum. In the light of these observations, one can understand the perceived disappearance of log-law in strong FPGs, alluded to by many researchers, as arising primarily due to their choice of the universal logarithmic law as the datum.

Figure 9 shows the sink flow profiles corresponding to figure 8 in defect coordinates (i.e. $(U - U_\infty)/U_\tau$ and y/δ). Similar features to those of figure 8 may be observed here pertaining to the outer intercept $-D$. It must be noted that each velocity profile

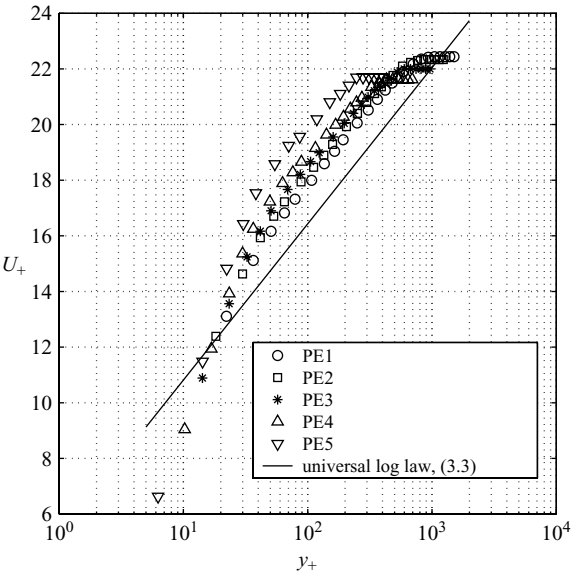

FIGURE 8. Mean velocity profiles in inner coordinates for different pressure gradients at station L4.

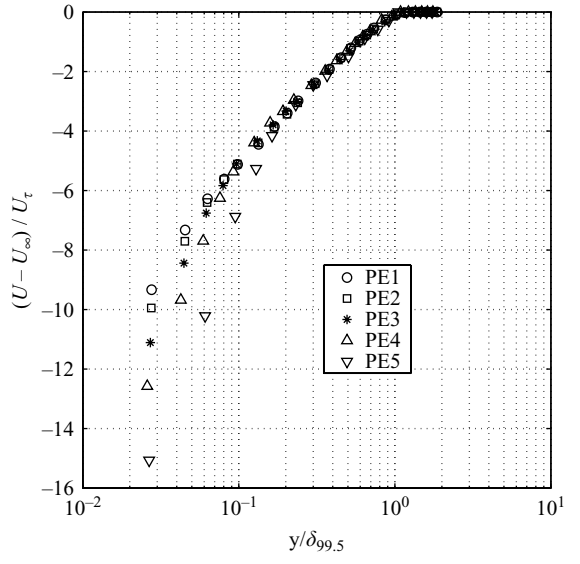

FIGURE 9. Mean velocity profiles in defect coordinates for different pressure gradients at station L4.

has the same slope $1/\kappa$ in both inner and defect plots (i.e. figures 8 and 9), thereby confirming that this is indeed a logarithmic variation.

It is conceivable that these changes in slope and intercepts of both logarithmic laws (inner and defect) are related to the changes in the strength of the streamwise pressure gradient. The method of matched asymptotic expansions (Yajnik 1970; Van Dyke 1975; Afzal 1976; Afzal & Narasimha 1976; Panton 2007) has been

used to provide theoretical support for the pressure gradient dependence of these non-universal logarithmic laws. This analysis is given in the next section.

4. Analysis

Consider a two-dimensional, steady, incompressible turbulent boundary layer flow subjected to a pressure gradient in the streamwise direction. The equations of mean motion under the boundary layer approximation are

$$\frac{\partial U}{\partial x} + \frac{\partial V}{\partial y} = 0, \tag{4.1}$$

$$U\frac{\partial U}{\partial x} + V\frac{\partial U}{\partial y} = U_\infty \frac{\mathrm{d}U_\infty}{\mathrm{d}x} + \nu\frac{\partial^2 U}{\partial y^2} + \frac{\partial \tau}{\partial y}, \tag{4.2}$$

where x is the streamwise coordinate, y is the coordinate normal to the surface, U and V are the mean velocity components in the streamwise and wall-normal directions respectively, U_∞ is the free-stream velocity and $\tau = -\overline{u'v'}$ is the kinematic Reynolds shear stress. Standard boundary conditions (such as no-slip at the wall) are applicable. U_∞ and δ are the larger or outer scales while U_τ and ν/U_τ are the smaller or inner scales, where $U_\tau = \sqrt{\tau_w/\rho}$ is the friction velocity. In the present work, the boundary layer thickness δ is defined as the value of the wall-normal coordinate y corresponding to the velocity which is 99.5% of U_∞ and is denoted by $\delta_{99.5}$.

In view of the possible rapid streamwise variations of the mean flow quantities that can be expected in a sink flow, it is of interest to assess the validity of the boundary layer approximation itself and the relative importance of normal stress terms in the boundary layer equations. The streamwise pressure gradient introduces a streamwise length scale, denoted by L', which is defined as

$$L' = \frac{U_\infty}{(\mathrm{d}U_\infty/\mathrm{d}x)}. \tag{4.3}$$

The boundary layer approximation is expected to hold only if the length scale in the wall-normal direction, which is the boundary layer thickness δ, is much smaller than L', i.e.

$$\frac{\delta}{L'} = \frac{\delta}{U_\infty}\frac{\mathrm{d}U_\infty}{\mathrm{d}x} \ll 1. \tag{4.4}$$

Condition (4.4) can be rewritten as

$$\frac{\delta}{L'} = \frac{\nu}{U_\infty^2}\frac{\mathrm{d}U_\infty}{\mathrm{d}x}\frac{U_\infty \delta}{\nu} = K R_\delta \ll 1, \tag{4.5}$$

where K and R_δ are both separately constants in the case of a sink flow TBL. Thus if the product $K R_\delta$ is much smaller than unity, then the boundary layer approximation is valid. Table 3 shows that for all the present experiments, this is indeed the case.

The Reynolds normal stress gradient terms, in the present experiments, would be almost two orders of magnitude smaller than the corresponding Reynolds shear stress gradient term. The following order of magnitude estimate illustrates this point:

$$\frac{\partial \overline{u'^2}}{\partial x} \sim \frac{\partial \overline{v'^2}}{\partial x} \sim \frac{U_\tau^2}{L'} \quad \text{and} \quad \frac{\partial \overline{u'v'}}{\partial y} \sim \frac{U_\tau^2}{\delta}, \tag{4.6a}$$

$$\therefore \quad \frac{\partial \overline{u'^2}/\partial x}{\partial \overline{u'v'}/\partial y} \sim \frac{\partial \overline{v'^2}/\partial x}{\partial \overline{u'v'}/\partial y} \sim \frac{\delta}{L'} \approx \frac{14}{1000}. \tag{4.6b}$$

Data set	K	C_f	Δ_p	$R_{\delta_{99.5}}$	δ/L'	$\epsilon = 1/[R_{\delta_{99.5}}(C_f/2)]$
PE1	7.71×10^{-7}	0.00401	−0.0086	17924	0.0138	0.0279
PE2	9.45×10^{-7}	0.00403	−0.0104	15061	0.0142	0.0329
PE3	1.23×10^{-6}	0.00416	−0.0129	11652	0.0143	0.0413
PE4	1.74×10^{-6}	0.00430	−0.0175	8021	0.0140	0.0581
PE5	2.90×10^{-6}	0.00433	−0.0288	4817	0.0140	0.0960

TABLE 3. Validity of the boundary layer approximation and justification for using the coefficient of viscous term in (4.9) as the perturbation parameter ϵ for the problem of outer layer.

4.1. *Outer layer formulation for sink flow*

For converting the system of partial differential equations (4.1) and (4.2) into an ordinary differential equation for the outer layer, we introduce the following outer variables:

$$\hat{U} = \frac{U}{U_\infty}, \quad \eta = \frac{y}{\delta}, \quad \hat{T} = \frac{\tau}{U_\tau^2}. \tag{4.7}$$

Introducing (4.7) into (4.1) gives a relation for the mean normal velocity V and substituting that along with (4.7) into (4.2) yields

$$\frac{\mathrm{d}\delta}{\mathrm{d}x}\left[-\frac{\mathrm{d}\hat{U}}{\mathrm{d}\eta}\int_0^\eta \hat{U}\,\mathrm{d}\eta\right] + \frac{\delta}{U_\infty}\frac{\mathrm{d}U_\infty}{\mathrm{d}x}\left[\hat{U}^2 - \frac{\mathrm{d}\hat{U}}{\mathrm{d}\eta}\int_0^\eta \hat{U}\,\mathrm{d}\eta - 1\right] = \frac{1}{R_\delta}\left[\frac{\mathrm{d}^2\hat{U}}{\mathrm{d}\eta^2}\right] + \left(\frac{U_\tau}{U_\infty}\right)^2\left[\frac{\mathrm{d}\hat{T}}{\mathrm{d}\eta}\right], \tag{4.8}$$

where the quantities $\mathrm{d}\delta/\mathrm{d}x$, $(\delta/U_\infty)\mathrm{d}U_\infty/\mathrm{d}x$, U_τ/U_∞ and $1/R_\delta$ must all become independent of the streamwise coordinate x for achieving self-similarity in terms of outer variables (4.7). The first condition, of constancy of $\mathrm{d}\delta/\mathrm{d}x$ with respect to x, indicates that the boundary layer thickness must vary linearly with the streamwise coordinate x. The second condition, $(\delta/U_\infty)\mathrm{d}U_\infty/\mathrm{d}x = K R_\delta =$ constant with respect to x, then gives a power law distribution for the free-stream velocity. The third condition, of constancy of U_τ/U_∞ with respect to x, implies that the skin friction coefficient $C_f = 2(U_\tau/U_\infty)^2$ must be invariant with x, giving a power law distribution for the friction velocity as well. The fourth and the last condition, $1/R_\delta =$ constant with x, connects the variations of U_∞ and δ (i.e. it relates the first and the second conditions) restricting the self-preserving solution only to the sink flow configuration. It has been demonstrated in § 3.1 (see figures 4*a*, 4*b* and 5*a*) that all the four conditions mentioned above are indeed fulfilled by the TBLs in the present sink flow experiments. Also, the mean velocity profile of a sink flow TBL exhibits self-similarity in conventional coordinates, in addition to the usual defect coordinates (shown before in § 3.1) and this observation is entirely consistent with (4.8).

For the sink flow configuration, (4.8) then reduces to

$$\beta[1 - \hat{U}^2] = \frac{1}{R_\delta(C_f/2)}\left[\frac{\mathrm{d}^2\hat{U}}{\mathrm{d}\eta^2}\right] + \left[\frac{\mathrm{d}\hat{T}}{\mathrm{d}\eta}\right], \tag{4.9}$$

where $\beta = (\delta/\rho U_\tau^2)\mathrm{d}p/\mathrm{d}x$ is the outer pressure gradient parameter and is proportional to the pressure gradient parameter $\beta_c = (\delta^*/\rho U_\tau^2)\mathrm{d}p/\mathrm{d}x$ of Clauser (1956). Equation (4.9) is the outer layer ODE for a sink flow TBL.

It is proposed to use the coefficient of the viscous term in (4.9) as the perturbation parameter ϵ for the outer layer problem in the asymptotic analysis. Towards this end,

we invoke the evidence from the present sink flow experiments as shown in table 3. It can be seen that the maximum strength of the viscous term (for the strongest FPG case PE5) is at most 10% of the strength of the Reynolds stress term. This suggests that the dynamics of the outer layer is still largely governed by the Reynolds stress term. This justifies the choice of the coefficient of the viscous term as the perturbation parameter ϵ for the outer layer problem.

The asymptotic expansions for the outer layer dependent variables (4.7) are now written

$$\hat{U} = 1 + \epsilon \hat{U}_1 + \cdots, \tag{4.10a}$$

$$\hat{T} = \hat{T}_0 + \epsilon \hat{T}_1 + \cdots, \tag{4.10b}$$

where $\epsilon = \epsilon(R_\delta, \beta)$ is the first outer gauge function and $\hat{U}_n(\eta)$, $\hat{T}_n(\eta)$ are coefficients, $\hat{U}_0(\eta)$ being taken as unity. By substituting the expansions (4.10) into (4.9), approximations of different orders to the outer layer ODE (4.9) may be obtained. These are given in Appendix A.

4.2. *Inner layer formulation for sink flow*

The inner variables are defined in the usual fashion as

$$U_+ = \frac{U}{U_\tau}, \quad y_+ = \frac{yU_\tau}{\nu}, \quad T_+ = \frac{\tau}{U_\tau^2}. \tag{4.11}$$

Using these inner variables (4.11), the mass conservation equation (4.1) and the mean streamwise momentum equation (4.2) together yield

$$\left[\frac{\mathrm{d}^2 U_+}{\mathrm{d}y_+^2}\right] + \left[\frac{\mathrm{d}T_+}{\mathrm{d}y_+}\right] - \Delta_p \left[1 - \left(\frac{C_f}{2}\right) U_+^2\right] = 0. \tag{4.12}$$

Here the third condition from the outer layer analysis, regarding the streamwise constancy of C_f, has been used to combine the pressure gradient term and the advective terms. From (4.12), we see that for the inner layer to be self-preserving, the inner pressure gradient parameter Δ_p must be independent of x. Now Δ_p may be rewritten as $\Delta_p = -K/(C_f/2)^{3/2}$ where K is the acceleration parameter given by $K = (\nu/U_\infty^2)\mathrm{d}U_\infty/\mathrm{d}x$ (see (1.1) and (1.2)). The conditions of streamwise constancy of C_f and Δ_p thus lead to the condition $K =$ constant. Equation (4.12) is the inner layer ODE for a sink flow TBL.

The asymptotic expansions for the inner layer dependent variables (4.11) are now written

$$U_+ = U_{0+} + \Gamma U_{1+} + \cdots, \tag{4.13a}$$

$$T_+ = T_{0+} + \Gamma T_{1+} + \cdots, \tag{4.13b}$$

where $\Gamma = \Gamma(\Delta_p)$ is the first inner gauge function, yet to be specified, and $U_{n+}(y_+)$ and $T_{n+}(y_+)$ are coefficients. By substituting the expansions (4.13) into (4.12), approximations of various orders to the inner layer ODE (4.12) may be obtained. These are given in Appendix A.

4.3. *Lowest-order asymptotic matching*

At sufficiently large Reynolds numbers, the outer limit of the inner description should match with the inner limit of the outer description according to the so-called Millikan–Kolmogorov matching principle (see Millikan 1938; Afzal & Narasimha 1976). As a first step, we match the two-term outer expansion (from (4.10)) of the mean velocity

with the corresponding one-term inner expansion (from (4.13)) as

$$\lim_{\eta\to 0} U_\infty(1+\epsilon\hat{U}_1) \sim \lim_{y_+\to\infty} U_\tau\,(U_{0+})\,. \tag{4.14}$$

Differentiating both sides with respect to y, for matching the gradients, gives

$$\lim_{\eta\to 0} \frac{\epsilon U_\infty}{U_\tau}\left(\eta\frac{\mathrm{d}\hat{U}_1}{\mathrm{d}\eta}\right) \sim \lim_{y_+\to\infty}\left(y_+\frac{\mathrm{d}U_{0+}}{\mathrm{d}y_+}\right). \tag{4.15}$$

If in (4.15) we have

$$\frac{\epsilon U_\infty}{U_\tau} = P_0 = O\,(1)\,, \tag{4.16}$$

as the experimental evidence suggests (see table 5), then each side of (4.15) must approach a constant value, say $1/\kappa_0$, which is independent of both η and y_+. That is,

$$\lim_{\eta\to 0} P_0\left(\eta\frac{\mathrm{d}\hat{U}_1}{\mathrm{d}\eta}\right) = \lim_{y_+\to\infty}\left(y_+\frac{\mathrm{d}U_{0+}}{\mathrm{d}y_+}\right) = \frac{1}{\kappa_0}. \tag{4.17}$$

Noting that P_0 is independent of both η and y_+, (4.17) may now be integrated separately on both sides to give

$$\hat{U}_1 = \frac{1}{P_0\kappa_0}\ln(\eta) - D_0', \tag{4.18}$$

$$U_{0+} = \frac{1}{\kappa_0}\ln(y_+) + C_0. \tag{4.19}$$

Here $1/\kappa_0$, C_0, D_0' and P_0 are all constants.

Putting (4.18) in the two-term outer expansion and (4.19) in the one-term inner expansion and simplifying yields, respectively,

$$\frac{U-U_\infty}{U_\tau} = \left[\frac{1}{\kappa_0}\right]\ln(\eta) - [P_0 D_0'], \tag{4.20}$$

$$U_+ = \left[\frac{1}{\kappa_0}\right]\ln(y_+) + [C_0]\,. \tag{4.21}$$

Note that the constants $1/\kappa_0$ and C_0 may be considered to be the same as those for a ZPG turbulent boundary layer (see (3.3)) since no pressure gradient information was used when deriving (4.20) and (4.21).

4.4. *Higher-order asymptotic matching*

First it is necessary to justify the need for higher-order matching. It has been mentioned in § 1 that the essential feature of strong pressure gradient TBL flows is the existence of a substantial gradient of total shear stress in the near-wall region. This is to be contrasted with the classical constant-stress region in ZPG or mild-pressure-gradient TBL flows. Higher-order matching essentially brings out this aspect explicitly (see Appendix A).

Let us now consider the matching of the three-term outer expansion (from (4.10)) of the mean velocity with the corresponding two-term inner expansion (from (4.13)) as

$$\lim_{\eta\to 0} U_\infty(1+\epsilon\hat{U}_1+\epsilon^2\hat{U}_2) \sim \lim_{y_+\to\infty} U_\tau(U_{0+}+\Delta_p U_{1+}). \tag{4.22}$$

Here the sequence of gauge functions in the outer expansion (4.10) is assumed to be a sequence of integral powers of ϵ and that in the inner expansion (4.13) is assumed to be a sequence of integral powers of Δ_p. Differentiation of (4.22) on both sides with respect to y gives

$$\lim_{\eta\to 0}\frac{\epsilon U_\infty}{U_\tau}\left(\eta\frac{\mathrm{d}\hat{U}_1}{\mathrm{d}\eta}+\epsilon\eta\frac{\mathrm{d}\hat{U}_2}{\mathrm{d}\eta}\right)\sim\lim_{y_+\to\infty}\left(y_+\frac{\mathrm{d}U_{0+}}{\mathrm{d}y_+}+\Delta_p y_+\frac{\mathrm{d}U_{1+}}{\mathrm{d}y_+}\right). \tag{4.23}$$

In view of (4.16) and (4.17), (4.23) reduces to

$$\lim_{\eta\to 0}\frac{P_0\epsilon}{\Delta_p}\left(\eta\frac{\mathrm{d}\hat{U}_2}{\mathrm{d}\eta}\right)\sim\lim_{y_+\to\infty}\left(y_+\frac{\mathrm{d}U_{1+}}{\mathrm{d}y_+}\right). \tag{4.24}$$

Now in (4.24) if we have

$$\frac{P_0\epsilon}{\Delta_p}=P_1=O(1), \tag{4.25}$$

as the experimental evidence suggests (see table 5), then each side of (4.24) must approach a constant value, say $1/\kappa_1$, which is independent of both η and y_+. That is,

$$\lim_{\eta\to 0}P_1\left(\eta\frac{\mathrm{d}\hat{U}_2}{\mathrm{d}\eta}\right)=\lim_{y_+\to\infty}\left(y_+\frac{\mathrm{d}U_{1+}}{\mathrm{d}y_+}\right)=\frac{1}{\kappa_1}. \tag{4.26}$$

Equation (4.26) on separate integrations of both sides now gives

$$\hat{U}_2=\frac{1}{P_1\kappa_1}\ln(\eta)-D_1', \tag{4.27}$$

$$U_{1+}=\frac{1}{\kappa_1}\ln(y_+)+C_1, \tag{4.28}$$

where $1/\kappa_1$, C_1, D_1' and P_1 are all constants.

Putting (4.18) and (4.27) in the three-term outer expansion and (4.19) and (4.28) in the two-term inner expansion for the streamwise mean velocity and simplifying yields

$$\frac{U-U_\infty}{U_\tau}=\left[\frac{1}{\kappa_0}+\Delta_p\frac{1}{\kappa_1}\right]\ln(\eta)-[P_0D_0'+\Delta_pP_1D_1'], \tag{4.29}$$

$$U_+=\left[\frac{1}{\kappa_0}+\Delta_p\frac{1}{\kappa_1}\right]\ln(y_+)+[C_0+\Delta_pC_1]. \tag{4.30}$$

Equations (4.29) and (4.30) are significant because they explicitly show the dependence of the slope and the intercepts in both the logarithmic laws on the pressure gradient parameter Δ_p for a sink flow TBL. It is possible to extend this matching procedure to still higher orders as necessitated by the demands of the problem. As will be shown in the next section, it is sufficient to extend the matching process to second order. The resulting mean velocity profiles are seen to be of a non-universal log-law form as given by

$$\frac{U-U_\infty}{U_\tau}=\frac{1}{\kappa}\ln(\eta)-D, \tag{4.31}$$

$$U_+=\frac{1}{\kappa}\ln(y_+)+C, \tag{4.32}$$

where

$$\frac{1}{\kappa} = \sum_{m=0}^{2} \Delta_p^m \frac{1}{\kappa_m}, \quad D = \sum_{m=0}^{2} \Delta_p^m P_m D'_m, \quad C = \sum_{m=0}^{2} \Delta_p^m C_m. \tag{4.33}$$

Some more comments about the outer additive constant $-D$ are in order. Equation (4.33) shows that

$$D = P_0 D'_0 + \Delta_p P_1 D'_1 + \Delta_p^2 P_2 D'_2, \tag{4.34}$$

where $P_0 = \epsilon U_\infty / U_\tau$, $P_1 = P_0 \epsilon / \Delta_p$ and $P_2 = P_1 \epsilon / \Delta_p$. It must be noted that P_0, P_1 and P_2 are themselves functions of Δ_p whereas D'_0, D'_1 and D'_2 are constants, presumably universal. The experimental evidence, as shown in figure 10 in § 5, suggests that these order-one quantities P_0, P_1 and P_2 are linear functions of Δ_p to a good approximation. The data for P_2 show mild oscillatory behaviour about the mean line but that is considered insignificant. Hence

$$P_0 = P'_0 + \Delta_p P''_0, \quad P_1 = P'_1 + \Delta_p P''_1, \quad P_2 = P'_2 + \Delta_p P''_2, \tag{4.35}$$

where primes do *not* indicate differentiation. Putting (4.35) in (4.34) gives

$$D = D_0 + \Delta_p D_1 + \Delta_p^2 D_2 + \Delta_p^3 D_3, \tag{4.36}$$

where $D_0 = P'_0 D'_0$, $D_1 = (P''_0 D'_0 + P'_1 D'_1)$, $D_2 = (P''_1 D'_1 + P'_2 D'_2)$ and $D_3 = P''_2 D'_2$. The cubic term in (4.36) can be left out since a quadratic in Δ_p is sufficient to correlate the data as shown in the next section.

Thus (4.33), in view of (4.36), may now be conveniently rewritten as

$$\frac{1}{\kappa} = \sum_{m=0}^{2} \Delta_p^m \frac{1}{\kappa_m}, \quad D = \sum_{m=0}^{2} \Delta_p^m D_m, \quad C = \sum_{m=0}^{2} \Delta_p^m C_m, \tag{4.37}$$

where the constants $1/\kappa_m$, C_m and D_m must be determined from a curve fit to the experimental data.

The non-universal skin friction law now follows from (4.31) and (4.32) as

$$\frac{U_\infty}{U_\tau} = \frac{1}{\kappa} \ln(\delta_+) + C + D. \tag{4.38}$$

Equations (4.31) and (4.32) are thus the pressure-gradient-dependent logarithmic laws for a sink flow TBL and (4.38) is the consequent pressure-gradient-dependent skin friction law.

The following two points are pertinent to the analysis presented above. First, the results presented above are strictly valid in the infinite-Reynolds-number limit. We have also pursued the finite-Reynolds-number corrections to these results and these are presented in Appendix C. Therein it is shown that for finite Reynolds numbers, even though the inner and defect profiles are not strictly logarithmic, the contribution of the additional non-logarithmic terms is insignificant. Thus the infinite-Reynolds-number results still represent a good approximation to the finite-Reynolds-number situation for the sink flow TBL.

Secondly, for a given sink flow (i.e. fixed values of δ_+ and Δ_p) the skin friction law (4.38) clearly shows that the friction velocity is proportional to the free-stream velocity i.e. $U_\tau \propto U_\infty$. In view of this, the defect law scaling $(U - U_\infty)/U_\tau = F_1(\eta)$ could equally well have been recast in terms of the free-stream velocity as $(U - U_\infty)/U_\infty = F_2(\eta)$. In this connection, the work of George & Castillo (1997) is relevant. Based on the full-similarity of the inner and outer governing equations in the limit of $Re \to \infty$, they show that the appropriate velocity scale for the defect velocity in the outer region of

the ZPG turbulent boundary layer is U_∞. Even though the idea of equilibrium used in the present work is different from that employed by George & Castillo (1997) (the so-called asymptotic invariance principle), the defect law scaling is identical for a sink flow TBL in both these approaches. We believe that this is because of the special nature of the sink flow with its unique invariance properties discussed above.

4.5. *The pressure gradient velocity scale U_p*

Since we have been considering strong FPGs, one natural question that arises is the relevance of the velocity scale which the pressure gradient itself introduces. Let us define this velocity scale U_p, similar to what is done for APG flows close to separation (see e.g. Nickels 2004) as

$$U_p^3 = -\frac{\nu}{\rho}\frac{\mathrm{d}p}{\mathrm{d}x} = \nu U_\infty \frac{\mathrm{d}U_\infty}{\mathrm{d}x}. \tag{4.39}$$

Rearranging (4.39), it is easy to show that

$$U_p = K^{1/3} U_\infty, \quad U_p = (-\Delta_p)^{1/3} U_\tau. \tag{4.40}$$

Since both K and Δ_p are constants for a sink flow TBL, U_p is always proportional to both U_∞ and U_τ. In view of this, U_p could have been used as the velocity scale in both the inner and defect law formulations in lieu of U_τ. However the magnitude of U_p varies from a minimum of about 20% of U_τ to a maximum of about 30% of U_τ, for the range of pressure gradients covered in the present study. In view of this, U_τ is used as the velocity scale in this work.

5. Comparison of the analysis with the present experiments and with other sink flow data in the literature

The following sink flow data sets are taken from various sources for making a comparison with the data from the present experiments in the light of the analysis of § 4. One representative data set is taken from the sink flow experiments of Jones *et al.* (2001). This corresponds to $K = 5.39 \times 10^{-7}$ and $\Delta_p = -0.00528$, which is their strongest pressure gradient case. This pressure gradient is still weaker than the weakest pressure gradient (case PE1) in the present experiments. Three sink flow DNS data sets of Spalart (1986) are also included.

The following procedure was adopted for finding the constants in the logarithmic laws. Inner logarithmic laws were fitted to the logarithmic portions of all the mean velocity profiles in figure 8 using the least squares fit. The slope $1/\kappa$ and the inner intercept C were thus readily obtained. Intercept $-D$ in the outer logarithmic law was then calculated from the skin friction law (4.38) by making use of the measured value of skin friction coefficient and was verified by visual inspection. This procedure was applied to all the data sets (listed in table 4) for the sake of uniformity. The procedure mentioned above can be made more systematic, as explained in Appendix B. Values of various important parameters for all these profiles are listed in table 4. As mentioned above, the values for the present experiments are averaged over last three stations L3, L4 and L5. For this reason, there might be slight differences between the values of these parameters as shown in table 4 and as seen in figures 8 and 9.

The analysis presented in § 4 contains the quantities P_0, P_1 and P_2 which are assumed to be of order one. Table 5 presents the evidence regarding the validity of this assumption. Also figure 10 shows the validity of linear approximation (4.35) for these order-one quantities.

Data set	Δ_p	C_f	κ	C	D	R_θ	R_{δ^*}
PE1	−0.0086	0.00401	0.4257	6.9600	−0.3257	1337	1794
PE2	−0.0104	0.00403	0.4382	7.6655	−0.2603	1119	1516
PE3	−0.0129	0.00416	0.4544	8.2886	−0.1703	879	1215
PE4	−0.0175	0.00430	0.4792	9.3096	−0.0820	612	889
PE5	−0.0288	0.00433	0.5002	10.6033	+0.0883	393	614
JMP3	−0.0053	0.00437	0.4204	5.4031	−0.3550	1573	2118
S1	−0.0120	0.00499	0.3960	5.2207	−0.5800	691	985
S2	−0.0188	0.00522	0.4443	7.3136	−0.4570	421	639
S3	−0.0202	0.00530	0.4397	7.2082	−0.3260	384	592

TABLE 4. Constants in logarithmic laws. PE denotes present experiments, JMP denotes Jones *et al.* (2001) and S denotes Spalart (1986).

Data set	C_f	$R_{\delta_{99.5}}$	ϵ	Δ_p	P_0	P_1	P_2
PE1	0.00401	17924	0.0279	−0.0086	0.62	−2.02	6.56
PE2	0.00403	15061	0.0329	−0.0104	0.73	−2.32	7.33
PE3	0.00416	11652	0.0413	−0.0129	0.91	−2.90	9.28
PE4	0.00430	8021	0.0581	−0.0175	1.25	−4.16	13.81
PE5	0.00433	4817	0.0960	−0.0288	2.06	−6.88	22.92
JMP3	0.00437	20739	0.0221	−0.0053	0.47	−1.97	8.22
S1	0.00499	8848	0.0453	−0.0120	0.91	−3.42	12.92
S2	0.00522	5574	0.0687	−0.0188	1.34	−4.91	17.96
S3	0.00530	4829	0.0781	−0.0202	1.52	−5.87	22.68

TABLE 5. Gauge functions and order-one quantities in the asymptotic analysis of § 4 for various data sets used in this study. See table 4 for data set abbreviations.

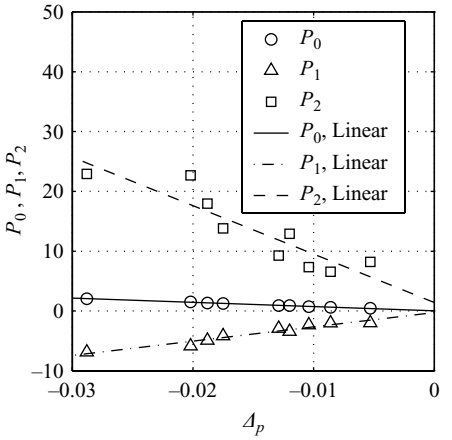

FIGURE 10. Linearity of order-one quantities P_0, P_1 and P_2 of § 4 with respect to Δ_p, plotted for cases listed in table 5.

Jones & Launder (1972) have presented experimental sink flow data. However it appears that their boundary layers were close to relaminarization. The values of shape factor H in the present experiments are in the range 1.34 to 1.56. On the other hand, for Jones & Launder (1972), the corresponding range is 1.42 to 1.76. This indicates that their mean velocity profiles are less full compared to those in the present experiments. Hence they may not be fully turbulent (i.e. they might be in a

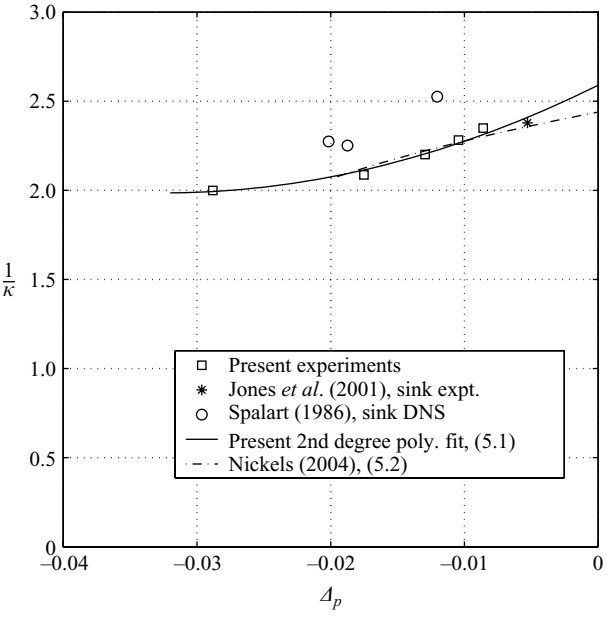

FIGURE 11. Slope $1/\kappa$ of logarithmic region versus Δ_p, for cases listed in table 4.

reverse-transitional state). Figure 2 from Jones & Launder (1972) clarifies this situation. Their experimental data points are much above the turbulent solution predicted using the method proposed by Launder & Jones (1969). Furthermore, the lowest value of R_θ in the present experiments is about 393 whereas the corresponding value for the data of Jones & Launder (1972) is about 310. Figure 1 from Jones & Launder (1972) again indicates that their experimental R_θ values are lower than those demanded by the turbulent sink flow solution. In view of these observations, the data of Jones & Launder (1972) have not been included in the present comparison.

As will be confirmed later in this section, strong pressure gradients indeed tend to alter the slope and the intercept of logarithmic region of the mean velocity profile considerably. For this reason, the method used for determining skin friction should not be based, in any way, on the universal logarithmic law. In view of this, the experimental FPG equilibrium turbulent boundary layer data of Herring & Norbury (1967) could not be used since the method used for skin friction measurement has not been mentioned. The calculations of Mellor & Gibson (1966) also make use of the universal logarithmic law for calculating the mean velocity profiles of equilibrium TBLs with pressure gradients and hence had to be left out.

5.1. *The slope $1/\kappa$ of the logarithmic region*

Figure 11 shows the slope $1/\kappa$ of the logarithmic region plotted against Δ_p. It is found that the extension of the asymptotic matching process to second order (see (4.37)) is sufficient to correlate the data from the present experiments including the experimental sink flow data point of Jones *et al.* (2001). The resulting second-degree polynomial fit, shown in figure 11, is given by

$$\frac{1}{\kappa} = \frac{1}{\kappa_0} + \Delta_p \frac{1}{\kappa_1} + \Delta_p^2 \frac{1}{\kappa_2}, \tag{5.1}$$

where $\kappa_0 = 0.3862$, $\kappa_1 = 0.02693$ and $\kappa_2 = 0.001753$.

The sink flow DNS data points of Spalart (1986) show a similar trend. However there are differences between the quadratic fit and the sink flow DNS data, especially pronounced for the DNS data S1; the DNS data are seen to collectively fall onto a curve distinct from the corresponding experimental points. The reason for this systematic departure in the trend seems to be related to the fact that the DNS mean velocity profiles are less full than the experiment profiles. This will be discussed further in § 5.4.

It can be seen from the trend of the present experiments that $1/\kappa$ is an increasing function of Δ_p. In order to heuristically understand this trend, we invoke some aspects of the so-called bursting events occurring close to the wall in a TBL. Bursting of low-speed streaks close to the wall is regarded as the physical mechanism of turbulence kinetic energy production (see Kline *et al.* 1967; Kim, Kline & Reynolds 1971). Observations indicate that while an APG makes the bursting phenomenon more vigorous, an FPG tends to suppress it. This implies that the production of turbulence kinetic energy is enhanced in an APG and is attenuated in an FPG. If so, then we may write $\mathrm{d}P_+/\mathrm{d}\Delta_p > 0$, where $P_+ = (-\overline{u'v'}/U_\tau^2)\mathrm{d}U_+/\mathrm{d}y_+$ is the turbulence kinetic energy production in inner scaling. If the boundary layer is turbulent, we may expect $(-\overline{u'v'})$ to scale on U_τ irrespective of the pressure gradient so that $(-\overline{u'v'}/U_\tau^2)$ is always of order one. In that case, the condition above can be rewritten as $\mathrm{d}(\mathrm{d}U_+/\mathrm{d}y_+)/\mathrm{d}\Delta_p > 0$, which in the overlap region (from (4.32)) becomes $\mathrm{d}(1/\kappa y_+)/\mathrm{d}\Delta_p > 0$. Now if we focus our attention on a fixed value of y_+, which always belongs to the overlap region (say $y_+ \approx 112$ in figure 8), then the above condition simplifies to $\left[\mathrm{d}(1/\kappa)/\mathrm{d}\Delta_p\right]_{y_+} > 0$. This implies that the slope $1/\kappa$ is indeed an increasing function of Δ_p.

Nickels (2004) has formulated a physical model for the turbulent boundary layer based on the idea of a universal critical Reynolds number for the viscous sublayer. This model yields

$$\frac{1}{\kappa} = \frac{1}{\kappa_0}\sqrt{1 + p_x^+ y_c^+}. \tag{5.2}$$

Here $p_x^+ = (\nu/\rho U_\tau^3)\mathrm{d}p/\mathrm{d}x$ is the non-dimensional pressure gradient parameter which is identical to Δ_p in the present analysis and y_c^+ is a non-dimensional sublayer thickness. Equation (5.2) is valid in the pressure gradient range $-0.02 < \Delta_p < 0.06$ for near-equilibrium and equilibrium TBL flows. The constant κ_0 (taken as 0.39 by Nickels 2004) is the value of κ corresponding to the ZPG case. The relation between y_c^+ and p_x^+ is given by Nickels (2004) as

$$p_x^+ y_c^{+3} + y_c^{+2} - R_c^2 = 0. \tag{5.3}$$

Equation (5.3) incorporates the linear variation of total stress in the near-wall region. $R_c = 12$ is the critical Reynolds number for the viscous sublayer, which is assumed to be a universal constant. Thus (5.2) essentially describes the variations in the slope of the logarithmic region depending on the pressure gradient, by taking the changes in sublayer thickness into account through (5.3).

In figure 11, (5.2) is plotted by taking $\kappa_0 = 0.41$ and it agrees fairly well with the present polynomial fit. It must be kept in mind that (5.2) takes the ZPG case into account while the present polynomial fit (5.1) does not. Hence differences are seen between (5.1) and (5.2) close to the $\Delta_p = 0$ line.

5.2. *The inner intercept C of the logarithmic region*

Figure 12 shows the inner intercept C of the logarithmic region plotted against Δ_p. Again the extension of the asymptotic matching process to second order (see (4.37))

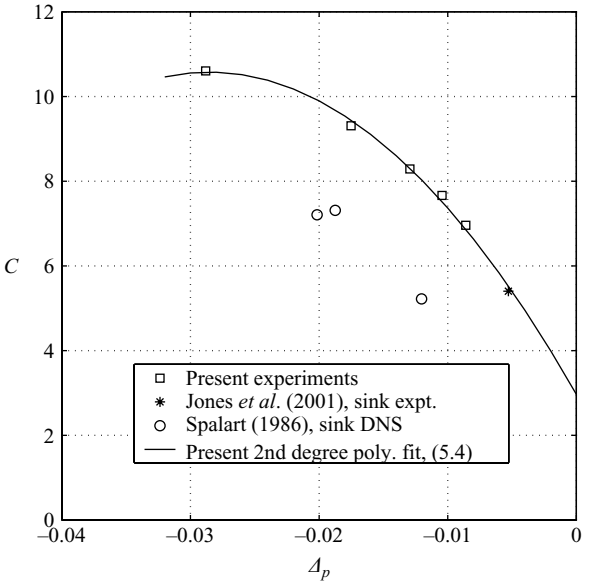

FIGURE 12. Inner intercept C of logarithmic region versus Δ_p, for cases listed in table 4.

is sufficient to correlate the experimental data points. The resulting second-degree polynomial fit, as seen in figure 12, is given by

$$C = C_0 + \Delta_p C_1 + \Delta_p^2 C_2, \tag{5.4}$$

where $C_0 = 2.9682$, $C_1 = -533.34$ and $C_2 = -9347.9$.

Here again the sink flow DNS data points of Spalart (1986) show a similar trend as before and there are systematic departures in this case also as in figure 11.

It must be emphasized here that the inner intercept C is related to the non-dimensional sublayer thickness, and for strong FPGs it is known that the sublayer thickness is relatively large (see Launder & Jones 1969). This can be seen from the mean velocity profiles of figure 8. This rise in the value of C, as seen in figure 12, with the increasing severity of the FPG is thus consistent with the corresponding thickening of the viscous sublayer.

5.3. *The outer intercept $-D$ of the logarithmic region*

Figure 13 shows negative of the outer intercept $-D$ of the logarithmic region plotted against Δ_p. Again the extension of the asymptotic matching process to second order (see (4.37)) is sufficient to correlate all the experimental data. The resulting second-degree polynomial fit, as seen in figure 13, is given by

$$D = D_0 + \Delta_p D_1 + \Delta_p^2 D_2, \tag{5.5}$$

where $D_0 = -0.5296$, $D_1 = -30.274$ and $D_2 = -302.46$.

The sink flow DNS data points of Spalart (1986) again show a similar trend and consistent departures, similar to those in figures 11 and 12.

5.4. *The shape factor H and the Clauser parameter G*

It is instructive to examine the behaviour of the shape factor $H = \delta^*/\theta$ and the so-called Clauser parameter G (to be defined in (5.9)), as the strength of the pressure gradient is varied. Clauser (1956), in his classic paper, derived the following relations.

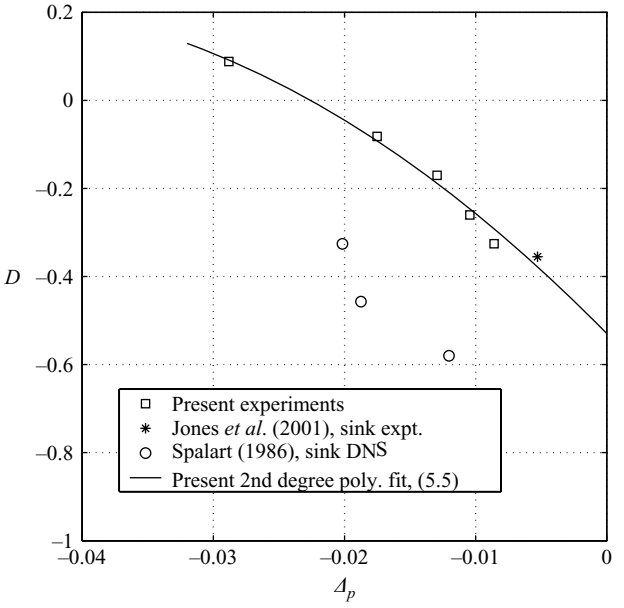

FIGURE 13. Negative of outer intercept $-D$ of logarithmic region versus Δ_p, for cases listed in table 4.

For self-similar defect profiles of a TBL

$$\frac{U - U_\infty}{U_\tau} = F\left(\frac{y}{\delta}\right), \tag{5.6}$$

where F is a function of the Clauser pressure gradient parameter β_c (mentioned in § 4.1). From (5.6), an integral thickness Δ can be defined as

$$\Delta = -\delta \int_0^\infty \left(\frac{U - U_\infty}{U_\tau}\right) \mathrm{d}\,(y/\delta)\,. \tag{5.7}$$

Now the relations between δ^*, θ and Δ can be shown to be

$$\frac{\delta^*}{\Delta} = \sqrt{\frac{C_f}{2}}, \quad \frac{\theta}{\Delta} = \sqrt{\frac{C_f}{2}}\left(1 - G\sqrt{\frac{C_f}{2}}\right), \tag{5.8}$$

where

$$G = \int_0^\infty \left(\frac{U - U_\infty}{U_\tau}\right)^2 \mathrm{d}\,(y/\Delta)\,. \tag{5.9}$$

From (5.8), the conventional shape factor H can be written as

$$H = \frac{\delta^*}{\theta} = \left(1 - G\sqrt{\frac{C_f}{2}}\right)^{-1}. \tag{5.10}$$

The parameter G (referred to as the Clauser parameter here) takes a constant value for all profiles which possess the same function F, as defined by (5.6). In other words, G is a constant for a particular self-preserving TBL flow and depends only on the pressure gradient through the function F. In particular, for a ZPG turbulent boundary layer, $G = 6.8$ (see Clauser 1956).

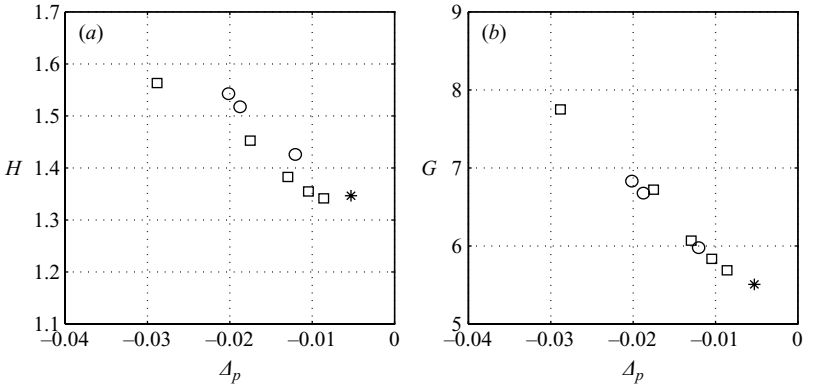

FIGURE 14. (*a*) Shape factor H versus Δ_p and (*b*) Clauser parameter G versus Δ_p, for cases listed in table 4. □, Present experiments; ○, Spalart (1986) sink DNS; ∗, Jones *et al.* (2001) sink experiment.

Note that the shape factor H, which is a measure of the fullness of the velocity profile, depends on the local skin friction coefficient (see (5.10)) even for nearly self-preserving TBL flows. This means that even if the mean velocity profiles show a collapse in the defect coordinates (i.e. $G =$ constant), H would vary with C_f. However, in the case of sink flow where there is exact self-preservation, H remains constant in the streamwise direction and changes only with the pressure gradient. Note that G also may be interpreted as a measure of the fullness of the mean velocity profile and is generally considered to be more convenient than H, for TBL flows. In fact, G could very well be considered as an indicator of the fullness of the *defect* velocity profile.

Figure 14(*a*) shows the shape factor H plotted against Δ_p for cases listed in table 4. For sink flows with mild FPGs, the values of H are low. As the magnitude of Δ_p increases, the value of H is seen to increase continuously, implying a continuous reduction in the fullness of the mean velocity profile. It is important to note that the DNS sink flow profiles of Spalart (1986) are relatively less full (relatively higher values of H) than those of the experimental data. This is believed to be the reason for the systematic departures of these DNS sink flow data sets from the corresponding trend of experiments in all the previous plots. This is also consistent with lower Reynolds numbers and higher skin friction values of the DNS data compared to those of the experiments (see table 4).

Figure 14(*b*) shows the behaviour of the Clauser parameter G for various sink flow cases given in table 4. It can be seen that all the data points fall on a single curve. This suggests that G may not be as appropriate an indicator of the fullness of the mean velocity profile as H. In general, the functional form of G could be expected to depend on the Coles wake factor Π (see Coles 1956) and the pressure gradient parameter Δ_p. To see this, consider the functional form of the defect velocity profile on the lines of (2.6) from Perry *et al.* (2002): $(U - U_\infty)/U_\tau = F_1(\eta, \Pi, \Delta_p)$. This can be integrated across the boundary layer (see (5.7) and (5.9) above) to yield $G = G(\Pi, \Delta_p)$ where the explicit Δ_p dependence comes about through the slope $1/\kappa$ and intercept $-D$ of the defect velocity profile. However, for a sink flow, $\Pi = 0$. This means that for different sink flow profiles $G = G(\Delta_p)$. This is the reason for the collapse of G values for different sink flows from experiments and DNS onto a single curve as seen in figure 14(*b*).

6. Conclusions

A systematic experimental study of sink flow turbulent boundary layers has been carried out over a wide range of streamwise pressure gradients. It is found that the mean velocity profiles (in inner coordinates) for these strong FPG flows exhibit systematic departures from the universal logarithmic law as the pressure gradient parameter Δ_p is varied. Even so, each of these mean velocity profiles exhibits a logarithmic region, albeit non-universal, whose constants are functions of the pressure gradient. Systematic dependence of these constants on the pressure gradient parameter Δ_p is observed. Moreover, the wake region is uniformly absent in all these profiles. In other words, each profile looks like a 'pure wall flow', in the sense of Coles (1957), only if it is viewed in relation to its own non-universal logarithmic law.

The method of matched asymptotic expansions has been applied to the sink flow turbulent boundary layer. This theory reveals a systematic dependence of inner and outer logarithmic laws on the pressure gradient parameter Δ_p. Comparison of the theory with the experimental data demonstrates that the disappearance of the universal logarithmic law in strong FPG situations does not necessarily imply the absence of a classical inner–outer overlap region. The overlap may still manifest itself as a logarithmic functional form with constants that are strongly influenced by the magnitude of FPG.

We would like to record our thanks to Professor P. Bradshaw for pointing out the literature on the surface hot-wire method for skin friction measurement and related discussions. Thanks are also due to Dr Tim Nickels for going through an earlier version of the manuscript and discussions.

Appendix A. Outer and inner equations of various orders

First, we have selected the sequence of gauge functions in the outer expansion (4.10) to be a sequence of integral powers of ϵ. Hence substituting (4.10) into (4.9) and collecting the coefficients of identical powers of ϵ gives

$$\frac{\mathrm{d}\hat{T}_0}{\mathrm{d}\eta} = 0, \text{ to lowest order,} \tag{A 1}$$

$$\frac{\mathrm{d}\hat{T}_1}{\mathrm{d}\eta} + 2\beta\hat{U}_1 = 0, \text{ to the next order.} \tag{A 2}$$

According to (A 1), to the lowest order, the Reynolds shear stress in the outer layer is constant with respect to y. This is consistent with the experimental observations that the mean velocity gradient does not change much over the outer layer and the eddy viscosity is almost constant in the outer layer (see e.g. Clauser 1956; Mellor & Gibson 1966; Townsend 1976). Equation (A 2) governs the Reynolds stress correction $\hat{T}_1$ of the next order occurring because of the combined effect of the pressure gradient and the next-order velocity correction $\hat{U}_1$. Viscous terms are of still higher order.

Next, we have selected the sequence of gauge functions in the inner expansion (4.13) to be a sequence of integral powers of Δ_p. Hence substituting (4.13) into (4.12) and collecting the coefficients of identical powers of Δ_p gives

$$\frac{\mathrm{d}^2U_{0+}}{\mathrm{d}y_+^2} + \frac{\mathrm{d}T_{0+}}{\mathrm{d}y_+} = 0, \text{ to lowest order,} \tag{A 3}$$

$$\frac{\mathrm{d}^2U_{1+}}{\mathrm{d}y_+^2} + \frac{\mathrm{d}T_{1+}}{\mathrm{d}y_+} = 1, \text{ to the next order.} \tag{A 4}$$

Here, in deriving (A 4), use has been made of (4.16) and (4.25).

Equation (A 3) shows that, to the lowest order, the total shear stress in the inner layer is constant with respect to y. Equation (A 4) however indicates that the next-order correction to the total stress varies linearly with y. It is this term which becomes important for strong pressure gradients. For almost all pressure gradients of practical interest, the total stress distribution is thus linear to a good approximation, consistent with the observations of Townsend (1956, 1976), Patel & Head (1968) and Nickels (2004). Hence it is clear that unless higher-order matching is done (see § 4.4), the gradient of total stress, which is an essential feature of the flows with strong pressure gradients, will not enter the analysis.

Appendix B. A systematic procedure for identifying the logarithmic region from experimental data

The presence of a logarithmic region in the mean velocity profile of a TBL is usually clear, especially in the case of a sink flow TBL, where the logarithmic region extends almost up to the mean edge of the boundary layer. Hence the extent of the logarithmic region could be decided simply by examining the inner profile by eye. However in order to avoid ambiguity and minimize the subjectivity involved, a rational procedure is required. This is described below.

In the logarithmic region, the mean velocity profile in inner coordinates is given by (4.32) as

$$U_+ = \frac{1}{\kappa}\ln(y_+) + C, \tag{B 1}$$

where $1/\kappa$ and C are functions of Δ_p but are constant with respect to y_+. Now differentiating (B 1) with respect to y_+ gives

$$y_+\frac{\mathrm{d}U_+}{\mathrm{d}y_+} = \frac{1}{\kappa}. \tag{B 2}$$

Following Spalart (1988), the quantity $y_+(\mathrm{d}U_+/\mathrm{d}y_+)$ from the mean velocity profile data is to be plotted against y_+. The logarithmic region can be identified as the extent of y_+ values over which the value of $y_+(\mathrm{d}U_+/\mathrm{d}y_+)$ is reasonably constant in a local plateau-like region. This method is applied to two representative data sets from the present experiments. The values of κ obtained by this method and by the least squares fit (which is used for all the data sets), are compared. One representative case from the sink flow DNS results of Spalart (1986) has also been evaluated using this procedure.

Figures 15(a) and 15(c) show the mean velocity profiles, in inner coordinates, for the present experiments PE1 and PE5 at station L4. Each profile is fitted with a cubic spline approximation from which the quantity $y_+(\mathrm{d}U_+/\mathrm{d}y_+)$ is evaluated at various values of y_+. Also shown in each figure is the region used for the least squares fit which is essentially decided by eye. It can be clearly seen that the quantity $y_+(\mathrm{d}U_+/\mathrm{d}y_+)$ is reasonably constant over the region where the least squares fit has been used. This confirms that there exists a logarithmic region, in each of the profiles of figure 15. Also, the extent of the plateau over which $y_+(\mathrm{d}U_+/\mathrm{d}y_+)$ is constant closely matches the extent of the least squares fit region. The average values of κ over this region may be obtained using (B 2), from figures 15(b) and 15(d). Figure 16(a, b) shows the results of the same procedure for the sink flow DNS (case S3) by Spalart (1986).

Referring to table 6, one can see that the differences in values of κ obtained from the least squares fit and from the above method are of the order of 2%. As estimated by Spalart (1988), the typical uncertainty in the value of κ is ± 0.01 for his DNS data. Results in table 6 agree very well with this estimate. This demonstrates that the least

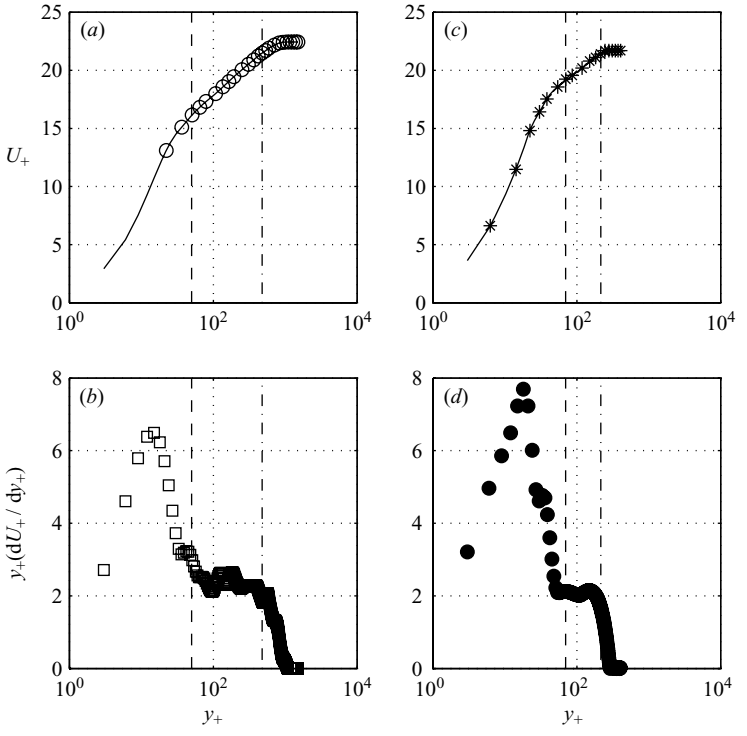

FIGURE 15. A systematic procedure for identification of the logarithmic region. (*a*) Mean velocity profile: ○, present experiment PE1 at station L4; ——, spline fit. (*b*) □, $y_+(\mathrm{d}U_+/\mathrm{d}y_+)$ versus y_+ from spline fit of (*a*). (*c*) Mean velocity profile: ∗, present experiment PE5 at station L4; ——, spline fit. (*d*) •, $y_+(\mathrm{d}U_+/\mathrm{d}y_+)$ versus y_+ from spline fit of (*c*); — — —, start of least squares fit region; —·—·, end of least squares fit region.

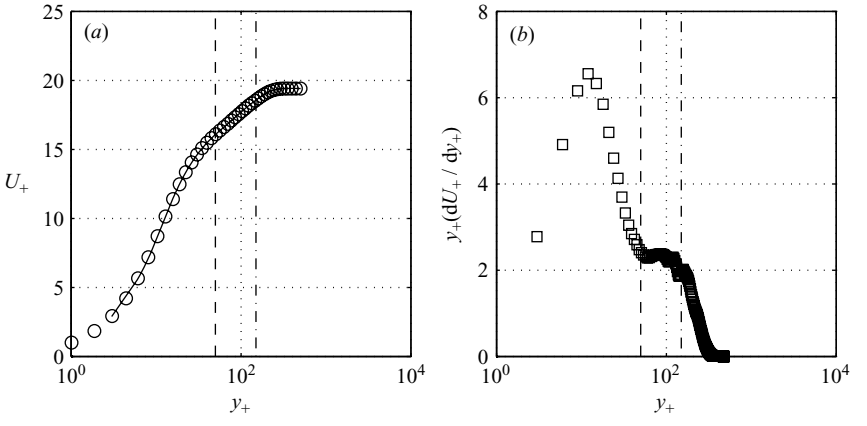

FIGURE 16. A systematic procedure for identification of the logarithmic region. (*a*) Mean velocity profile: ○, data set S3 listed in table 4; ——, spline fit. (*b*) □, $y_+(\mathrm{d}U_+/\mathrm{d}y_+)$ versus y_+ from spline fit of (*a*); — — —, start of least squares fit region; —·—·, end of least squares fit region.

Data set	κ from least squares fit	κ using (B 2)	% difference in κ with respect to least squares value
PE1	0.4212	0.4297	2
PE5	0.5008	0.4928	−1.6
S3	0.4397	0.4488	2

TABLE 6. Comparison of values of κ as obtained by the least squares fit and by using (B 2) for the cases shown in figures 15 and 16.

squares fit used for all the data sets gives reasonably acceptable and plausible values of κ.

Appendix C. Higher-order asymptotic matching with inclusion of finite-Reynolds-number effects

The asymptotic matching given in §§ 4.3 and 4.4 can be made more rational by including the finite-Reynolds-number effects. Afzal (1976), in his interesting paper, extended the asymptotic matching of inner and defect regions to the next order for turbulent pipe and channel flows. He used the result of Gill (1968) concerning the estimate of the error involved at the lowest level of matching. Following Afzal (1976), Buschmann & Gad-el-Hak (2003) extended the matching procedure to arbitrary orders and derived a generalized logarithmic law (which contains other non-logarithmic terms as well) that takes into account the effects of finite Reynolds number for a ZPG turbulent boundary layer flow. It is possible to apply the same methodology in the present case. In order to do so, consider (4.17) which in view of Gill (1968) becomes

$$\lim_{\eta\to 0} P_0\left(\eta\frac{\mathrm{d}\hat{U}_1}{\mathrm{d}\eta}\right) = \frac{1}{\kappa_0} + O\left(\eta^s\right), \tag{C 1}$$

$$\lim_{y_+\to\infty}\left(y_+\frac{\mathrm{d}U_{0+}}{\mathrm{d}y_+}\right) = \frac{1}{\kappa_0} + O(y_+^{-t}), \tag{C 2}$$

where $s > 0$ and $t > 0$. In view of (C 1) and (C 2), (4.18) and (4.19) can now be written as

$$\hat{U}_1 = \frac{1}{P_0\kappa_0}\ln(\eta) - D_0' + o(1), \tag{C 3}$$

$$U_{0+} = \frac{1}{\kappa_0}\ln(y_+) + C_0 + o(1). \tag{C 4}$$

The $o(1)$ quantities in (C 3) and (C 4) must be estimated, at least to their lowest order, before proceeding further with the matching of $O(\epsilon)$ terms in the expansions for mean velocity as is done is (4.22). In other words, the higher-order contribution of the lower-order result must be taken into account when higher-order matching is carried out. Following Afzal (1976), (C 3) and (C 4) may be rewritten as

$$\hat{U}_1 = \frac{1}{P_0\kappa_0}\ln(\eta) - D_0' + E_0\eta + \cdots \text{ as } \eta\to 0, \tag{C 5}$$

$$U_{0+} = \frac{1}{\kappa_0}\ln(y_+) + C_0 + \frac{F_0}{y_+} + \cdots \text{ as } y_+\to\infty, \tag{C 6}$$

where E_0 and F_0 are constants, essentially $O(1)$ (for the meaning of order symbols O and o, refer to Van Dyke 1975). Now (C 5) and (C 6) must be substituted in (4.23) to obtain a rational higher-order matching. When this is done, one obtains modified forms of (4.27) and (4.28) as

$$\hat{U}_2 = \frac{1}{P_1\kappa_1}\ln(\eta) - D_1' - \frac{E_0}{\epsilon}\eta + E_1\eta^2 + \cdots \text{ as } \eta \to 0, \tag{C 7}$$

$$U_{1+} = \frac{1}{\kappa_1}\ln(y_+) + C_1 - \frac{F_0}{\Delta_p}\frac{1}{y_+} + \frac{F_1}{y_+^2} + \cdots \text{ as } y_+ \to \infty, \tag{C 8}$$

where $E_1\eta^2$ and F_1/y_+^2 are the estimates of $o(\eta)$ and $o(1/y_+)$ quantities in (C 7) and (C 8) which have to be used for the next-order matching.

Proceeding in similar fashion to the next order and substituting the expressions for $\hat{U}_1$, $\hat{U}_2$ and $\hat{U}_3$ in the four-term outer expansion (from (4.10)) and the expressions for U_{0+}, U_{1+} and U_{2+} in the three-term inner expansion (from (4.13)) yields

$$\frac{U - U_\infty}{U_\tau} = \frac{1}{\kappa}\ln(\eta) - D + P_0E_2\epsilon^2\eta^3 \quad \text{as } \eta \to 0, \tag{C 9}$$

$$U_+ = \frac{1}{\kappa}\ln(y_+) + C + \frac{F_2\Delta_p^2}{y_+^3} \quad \text{as } y_+ \to \infty, \tag{C 10}$$

where

$$\frac{1}{\kappa} = \sum_{m=0}^{2}\Delta_p^m\frac{1}{\kappa_m}, \quad D = \sum_{m=0}^{2}\Delta_p^m D_m, \quad C = \sum_{m=0}^{2}\Delta_p^m C_m. \tag{C 11}$$

Equations (C 9) and (C 10) are general versions of (4.31) and (4.32), each including one additional non-logarithmic term that represents the effect of finite Reynolds number. This additional term is of the same order as the one up to which the matching procedure is extended. Also note that there are no additional lower-order terms.

It is instructive to plot (C 9) and (C 10) along with their pure logarithmic counterparts (4.31) and (4.32) in order to assess the effect of the non-logarithmic extra terms. It was decided to use the strongest pressure gradient experiment PE5 for this purpose since it contains the largest values of ϵ, Δ_p and P_0 (this will yield the largest values for the extra terms). Tables 3, 4 and 5 respectively show that $\epsilon = 0.096$, $\Delta_p = -0.02882$ and $P_0 = 2.06$ for case PE5. Further E_2 and F_2 are by definition $O(1)$ and for the present purpose they are arbitrarily chosen to be equal to unity.

Figures 17(a) and 17(b), for the present experiment PE5, respectively show a comparison of inner equations (C 10) and (4.32) and the defect equations (C 9) and (4.31). It is clear that the extra terms make no discernible difference. Also, if the value of E_2 is changed from 1 to 10, (C 9) and (4.31) are seen to be identical up to about $\eta = 0.1$ and thereafter show only slight differences towards the edge of the boundary layer. On the other hand (C 10) and (4.32) hardly differ from each other even for large changes in the value of F_2, say from 1 to 100. This demonstrates that the finite-Reynolds-number correction terms are in practice insignificant. Thus it appears that the infinite-Reynolds-number results (4.31) and (4.32) can be safely used for finite Reynolds number cases as well. Since the pressure gradient parameter Δ_p is related to the Reynolds number through C_f (see (1.2) and (4.38)), even the infinite Reynolds number results, in some sense, include the Reynolds number effects for a sink flow TBL.

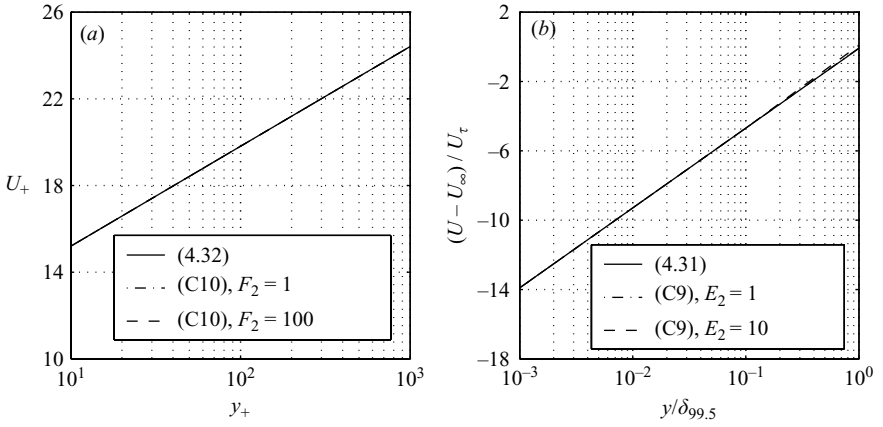

FIGURE 17. Influence of the extra non-logarithmic terms due to finite-Reynolds-number effects. (*a*) Comparison of the inner equations (4.32) and (C 10). (*b*) Comparison of the defect equations (4.31) and (C 9).

REFERENCES

AFZAL, N. 1976 Millikan's argument at moderately large Reynolds number. *Phys. Fluids* **19** (4), 600–602.

AFZAL, N. & NARASIMHA, R. 1976 Axisymmetric turbulent boundary layer along a circular cylinder at constant pressure. *J. Fluid Mech.* **74**, 113–128.

BRADSHAW, P. & FERRISS, D. H. 1965 The response of a retarded equilibrium turbulent boundary layer to the sudden removal of pressure gradient. *NPL Aero. Report* 1145.

BRADSHAW, P. & GREGORY, N. 1959 The determination of local turbulent skin-friction from observations in the viscous sublayer. *ARC London R&M* 3202.

BUSCHMANN, M. H. & GAD-EL-HAK, M. 2003 Generalized logarithmic law and its consequences. *AIAA J.* **41** (1), 40–48.

CLAUSER, F. H. 1954 Turbulent boundary layers in adverse pressure gradients. *J. Aero. Sci.* **21**, 91–108.

CLAUSER, F. H. 1956 The turbulent boundary layer. *Adv. Appl. Mech.* **4**, 1–51.

COLES, D. E. 1956 The law of the wake in the turbulent boundary layer. *J. Fluid Mech.* **1**, 191–226.

COLES, D. E. 1957 Remarks on the equilibrium turbulent boundary layer. *J. Aero. Sci.* **24**, 495–506.

FERNHOLZ, H. H. 2006 The role of skin-friction measurements in boundary layers with variable pressure gradients. In *IUTAM Symposium on One Hundred Years of Boundary Layer Research* (ed. G. E. A. Meier & K. R. Sreenivasan), pp. 231–240. Springer.

FERNHOLZ, H. H., JANKE, G., SCHOBER, M., WAGNER, P. M. & WARNACK, D. 1996 New developments and applications of skin-friction measuring techniques. *Meas. Sci. Technol.* **7**, 1396–1409.

FERNHOLZ, H. H. & WARNACK, D. 1998 The effects of a favourable pressure gradient and of the Reynolds number on an incompressible axisymmetric turbulent boundary layer. Part 1. The turbulent boundary layer. *J. Fluid Mech.* **359**, 329–356.

GEORGE, W. K. & CASTILLO, L. 1997 Zero-pressure-gradient turbulent boundary layer. *Appl. Mech. Rev.* **50** (12), 689–729.

GILL, A. E. 1968 The Reynolds number similarity argument. *J. Math. Phys.* **47**, 437–441.

HERRING, H. J. & NORBURY, J. F. 1967 Some experiments on equilibrium turbulent boundary layers in favourable pressure gradients. *J. Fluid Mech.* **27**, 541–549.

JONES, M. B., MARUSIC, I. & PERRY, A. E. 2001 Evolution and structure of sink-flow turbulent boundary layers. *J. Fluid Mech.* **428**, 1–27.

JONES, W. P. & LAUNDER, B. E. 1972 Some properties of sink-flow turbulent boundary layers. *J. Fluid Mech.* **56**, 337–351.

KIM, H. T., KLINE, S. J. & REYNOLDS, W. C. 1971 The production of turbulence near a smooth wall in a turbulent boundary layer. *J. Fluid Mech.* **50**, 133–160.

Kline, S. J., Reynolds, W. C., Schraub, F. A. & Runstadler, P. W. 1967 The structure turbulent boundary layers. *J. Fluid Mech.* **30**, 741–773.

Launder, B. E. & Jones, W. P. 1969 Sink flow turbulent boundary layers. *J. Fluid Mech.* **38**, 817–831.

MacMillan, F. A. 1956 Experiments on Pitot-tubes in shear flow. *ARC London R&M* 3028.

Mellor, G. L. & Gibson, D. M. 1966 Equilibrium turbulent boundary layers. *J. Fluid Mech.* **24**, 225–253.

Millikan, C. B. 1938 A critical discussion of turbulent flows in channels and circular tubes. In *Proc. 5th Intl Cong. Appl. Mech.* (ed. J. P. den Hartog & H. Peters), pp. 386–392. Wiley/Chapman & Hall.

Narasimha, R. & Sreenivasan, K. R. 1973 Relaminarization in highly accelerated turbulent boundary layers. *J. Fluid Mech.* **61**, 417–447.

Nickels, T. B. 2004 Inner scaling for wall-bounded flows subject to large pressure gradients. *J. Fluid Mech.* **521**, 217–239.

Panton, R. L. 2007 Composite asymptotic expansions and scaling wall turbulence. *Phil. Trans. R. Soc. Lond.* A**365**, 733–754.

Patel, V. C. 1965 Calibration of the Preston tube and limitations on its use in pressure gradients. *J. Fluid Mech.* **23**, 185–208.

Patel, V. C. & Head, M. R. 1968 Reversion of turbulent to laminar flow. *J. Fluid Mech.* **34**, 371–392.

Perry, A. E., Marusic, I. & Jones, M. B. 2002 On the streamwise evolution of turbulent boundary layers in arbitrary pressure gradients. *J. Fluid Mech.* **461**, 61–91.

Perry, A. E., Marusic, I. & Li, J. D. 1994 Wall turbulence closure based on classical similarity laws and the attached eddy hypothesis. *Phys. Fluids* **6**, 1024–1035.

Rotta, J. C. 1962 Turbulent boundary layers in incompressible flow. *Prog. Aeronaut. Sci.* **2**, 1–220.

Schlichting, H. & Gersten, K. 2000 *Boundary-Layer Theory*, 8th edn. Springer.

Spalart, P. R. 1986 Numerical study of sink flow boundary layers. *J. Fluid Mech.* **172**, 307–328.

Spalart, P. R. 1988 Direct simulation of a turbulent boundary layer up to $R_\theta = 1410$. *J. Fluid Mech.* **187**, 61–98.

Spalart, P. R. & Leonard, A. 1986 Direct numerical simulation of equilibrium turbulent boundary layers. In *Turbulent Shear Flows 5* (ed. F. J. Durst *et al.*), pp. 232–252. Springer.

Townsend, A. A. 1956 *The Structure of Turbulent Shear Flow*, 1st edn. Cambridge University Press.

Townsend, A. A. 1976 *The Structure of Turbulent Shear Flow*, 2nd edn. Cambridge University Press.

Van Dyke, M. 1975 *Perturbation Methods in Fluid Mechanics*. Stanford, CA: Parabolic Press.

Warnack, D. & Fernholz, H. H. 1998 The effects of a favourable pressure gradient and of the Reynolds number on an incompressible axisymmetric turbulent boundary layer. Part 2. The boundary layer with relaminarization. *J. Fluid Mech.* **359**, 357–381.

Yajnik, K. S. 1970 Asymptotic theory of turbulent shear flows. *J. Fluid Mech.* **42**, 411–427.